THESIS FOR THE DEGREE OF DOCTOR OF PHILOSOPHY

Behavior of iron-based oxygen carriers at deep reduction states

VICTOR PURNOMO

Department of Chemistry and Chemical Engineering

CHALMERS UNIVERSITY OF TECHNOLOGY

Gothenburg, Sweden 2024

Behavior of iron-based oxygen carriers at deep reduction states

VICTOR PURNOMO
ISBN 978-91-8103-009-9

Doktorsavhandlingar vid Chalmers tekniska högskola
Ny serie nr 5467
ISSN 0346-718X

Department of Chemistry and Chemical Engineering
Chalmers University of Technology
SE-412 96 Gothenburg
Sweden
Telephone + 46 (0)31-772 1000

Cover:
Illustration on how reactivity and physical phenomena may affect a single oxygen carrier particle at high degrees of reduction.
Top right: Reactivity follows the Changing Grain Size kinetic model and reduced iron oxide phases migrate toward the particle surface.
Bottom left: Attrition occurrence on the particle surface due to, for example, collision.

Printed by Chalmers Digitaltryck
Gothenburg, Sweden 2024

Behavior of iron-based oxygen carriers at deep reduction states

Victor Purnomo
Department of Chemistry and Chemical Engineering
Chalmers University of Technology

Abstract

Oxygen carriers have an important role as bed materials in both common circulating fluidized bed combustion unit (also known as oxygen-carrier-aided combustion, OCAC) and in various chemical looping processes. Contrary to conventional bed materials, e.g., sand, oxygen carriers are capable of transferring both oxygen and heat. This makes it possible to produce nitrogen-free product gas streams (in the case of chemical looping processes) and achieve a higher fuel conversion. Having been studied for almost three decades, various oxygen carriers show their own pros and cons depending on the processes for which they are intended to be used. Most of the published studies before this doctoral thesis focused on the reactivity and utilization of oxygen carriers in chemical looping combustion (CLC), where a complete fuel conversion is always desired. Nevertheless, this is not the case in, for example, chemical looping gasification, reforming, and water splitting, where only partial fuel oxidation is necessary, and the produced flue gases are the desired products. In such processes, the oxygen carriers can be exposed to a higher reduction degree than it would be in CLC or OCAC. This warrants further investigations into the deep reduction states of relevant oxygen carriers, which are expected to encounter inevitable performance issues under such a harsh environment.

In this thesis, some aspects related to the physical performance and properties of various iron-based oxygen carriers in the occurrence of deep reduction states are examined and presented. The first part of the thesis focuses on the fluidization performance, attrition resistance, and particle size and shape analysis. This part is important mainly for assessing material stability. Iron-based oxygen carriers typically tend to encounter bed defludization at a high degree of reduction. The outward migration of iron into the particle surface, which typically creates a FeO/Fe layer, likely causes defludization. Furthermore, the oxidation state of oxygen carriers does affect the attrition resistance of iron oxygen carriers to varying extents. The results indicate that the presence of Fe-Ti and Fe-Si combinations contribute to a generally stable and low attrition rate, while an Fe-Ca system exhibits a decreasing attrition rate. In addition, the influence of exposure to redox cycles and oxidation degree on the size and shape of oxygen carrier particles seems to be minimal. The oxygen carrier particles generally have a high sphericity but are slightly elongated.

Reactivity and fuel conversion are the other focuses of this thesis. These have main implications for engineering design but also for material screening. The apparent kinetic study of oxygen carrier performed in this thesis demonstrates that the changing grain size (CGS) model is applicable to predict the reactivity of three iron oxygen carriers in the presence of CO, H_2, and CH_4. This applies even at lower oxidation degrees (3 – 5 wt.% reduction), where the reactivity of oxygen carriers has generally decreased. Finally, the gasification rate of pine forest residue char remains at similar levels when using either ilmenite or iron sand as the oxygen carrier.

Keywords: oxygen carrier, iron oxides, deep reduction, physical performance, reactivity, fuel conversion, chemical looping

List of Publications

This thesis is based on the experimental studies reported in these articles:

Paper I
Purnomo, V., Yilmaz, D., Leion, H., Mattisson, T.
Study of defluidization of iron- and manganese-based oxygen carriers under highly reducing conditions in a lab-scale fluidized-bed batch reactor (2021)
Fuel Processing Technology, 219, 106874

Paper II
Purnomo, V., Mei, D., Soleimanisalim, A. H., Mattisson, T., Leion, H.
Effect of the Mass Conversion Degree of an Oxygen Carrier on Char Conversion and Its Implication for Chemical Looping Gasification (2022)
Energy & Fuels, 36, 17, 9768 – 9799

Paper III
Purnomo, V., Staničić, I., Mei, D., Soleimanisalim, A. H., Mattisson, T., Rydén, M., Leion, H.
Performance of iron sand as an oxygen carrier at high reduction degrees and its potential use for chemical looping gasification (2023)
Fuel, 339, 127310

Paper IV
Purnomo, V., Mei, D., Staničić, I., Mattisson, T., Leion, H.
Effect of oxidation degree on apparent kinetics of iron-based oxygen carriers
Submitted for publication

Paper V
Purnomo, V., Faust, R., Ejjeta, L. A., Mattisson, T., Leion, H.
Effect of oxidation degree of iron-based oxygen carriers on their mechanical strength
Submitted for publication

Paper VI
Purnomo, V., Takehara, M. D. B., Faust, R., Ejjeta, L. A., Leion, H.
New approach for particle size and shape analysis of iron-based oxygen carriers at different oxidation degrees (2024)
Particuology

Contribution report

Paper I	Principal author with main responsibility for all the experimental work, data collection, characterization work, and writing.
Paper II	Principal author with main responsibility for all the experimental work, data collection, characterization work, and writing.
Paper III	Principal author with main responsibility for all the experimental work, data collection, characterization work, and writing.
Paper IV	Principal author with main responsibility for performing parts of the experimental work, supervision of bachelor students who performed the rest of experimental work and data collection, characterization work, and writing.
Paper V	Principal author with main responsibility for supervision of the experimental work, data collection, and characterization performed by a research assistant and two bachelor students, and writing.
Paper VI	Principal author with main responsibility for supervision of the experimental work, data collection, and characterization performed by a research assistant, and writing. The particle size and shape analysis were carried out at Luleå University of Technology.

Related peer-reviewed papers not included in this thesis

Lidman Olsson, E. O., Purnomo, V., Glarborg, P., Leion, H., Dam-Johansen, K., Wu, H.
Thermal Conversion of Sodium Phytate Using the Oxygen Carrier Ilmenite Interaction with Na-Phosphate and Its Effect on Reactivity (2022)
Energy & Fuels, 36, 17, 9423 – 9436

Purnomo, V., Hildor, F., Knutsson, P., Leion, H.
Interactions between potassium ashes and oxygen carriers based on natural and waste materials at different initial oxidation states (2023)
Greenhouse Gases: Science and Technology, 13, 4, 520 – 534

Samprón, I., Purnomo, V., Mattisson, T., Leion, H., de Diego, L.F., García-Labiano, F.
Catalytic Activity of Oxygen Carriers on the Removal of Tar Byproducts for Biomass Chemical Looping Gasification Application (2023)
Energy & Fuels, 37, 21, 16629 – 16638

Acknowledgments

My earnest gratitude goes to my main supervisor, Henrik Leion, and my co-supervisors, Tobias Mattisson and Daofeng Mei. To Henrik, thank you for always believing in me even when everything seemed dark at some point in this PhD journey. You are certainly one of the kindest and most supportive supervisors I have ever had. To Tobias, your critical way of thinking always impresses and inspires me. Every manuscript that I had written always became much better after I applied your suggestions. I am proud to have been supervised by you. To Daofeng, I highly appreciate your earnest effort in supervising me. Your hard work is not only admirable but also inspiring. It is an honor to be the first doctoral student you have supervised officially in your academic career.

I would like to acknowledge the European Union's Horizon 2020 research and innovation program for having funded the project CLARA (Chemical Looping Gasification for Sustainable Production of Biofuels) under grant agreement No. 817841. Furthermore, the Swedish Energy Agency is acknowledged for funding the project 51430-1. Finally, funding from the ÅForsk Foundation to project 20-269 is also acknowledged.

I am thankful to have met all colleagues in both Energy Technology and Environmental Inorganic Chemistry for always creating a hospitable environment for me to learn and grow. To Xiaoyun and Nasrin, it is such a great joy to have embarked on this PhD journey side by side with you both as friends since we started this position in the same year. All the best for your coming dissertations! To Fredrik, Felicia, Ivana, and Viktor, I am glad to have worked in the same laboratory with you. I am looking forward to working with you again in the future. To Emil in Denmark, I will not forget your sincere encouragement during one of the most challenging times in my PhD study.

I am extremely blessed to have met my friends whom I highly treasure. To Faris, Annisa, Ridwan, Rahmatdi, Iqbaal, Eka, and Angie; thank you for the continuous moral support that I have received from you all. I will cherish all the great memories that we have had. To Albertus, I am delighted that our lasting friendship is still counting. Thank you for every single piece of advice and motivation you have given to me, and I look forward to exploring the world again with you.

Finally, I would not be standing here without the steadfast support from my late mom, whom I love the most. To my dearest siblings, Linda and Daniel, thanks for always being there for me, I hope I can meet you both soon! To Gracia, my partner who understands me the most, thank you for always believing in me. I cherish your unwavering support and look forward to sharing the future with you.

Victor Purnomo
Göteborg, February 2024

Table of Contents

1. Introduction

1.1 Background

Since the beginning of the industrialization era, the quality of human lives has improved significantly in many aspects. While perceived as an advantage, such an advancement unfortunately comes with serious consequences. This is because the rapid development of industries leads to a higher emission of greenhouse gases, in particular carbon dioxide. The unprecedented accumulation of carbon dioxide in the atmosphere keeps heat from escaping the atmosphere, which in turns leads to the global temperature increase and, subsequently, climate change. Both these phenomena threatens the longevity of life on earth in many aspects [1]. As a result, catastrophes and natural disasters occur more frequently than in the past [2]. These include the most recent calamities, such as extreme rainfalls that cause disastrous floods and unprecedented heatwaves that lead to uncontrollable wildfires. These phenomena are happening more frequently nowadays and becoming a new normal [3]. The outcomes of our increasing carbon footprint are literally in our own backyards; therefore, it is important to address this issue in a scientifically proven and efficient way.

We have the possibility to modify our engineering products to be environmentally sound and more sustainable. Carbon capture technology is considered one of the most plausible ways to avoid carbon dioxide release into the atmosphere. This should allow the sequestration of carbon dioxide in geological carbon storages, e.g., under the seabed [4], so the accumulation of carbon dioxide in the atmosphere can be minimized and the climate change effect can gradually be reversed. There are currently multiple strategies to establish this aim. One of them is to commercialize energy conversion processes, such as combustion and gasification, with the possibility for carbon capture [5,6].

1.1.1 Chemical looping technology and oxygen carrier aided combustion

One of the most prevalent issues with carbon capture is costly gas separation. This is because separating CO_2 from the flue gas, also known as post-combustion carbon capture, tends to be expensive and energy intensive [7,8]. Furthermore, the dilution of nitrogen in the flue gas makes the carbon capture process less beneficial [9]. Alternatively, separating nitrogen from air before combustion can be a solution. This will lead to nitrogen-free combustion. However, the currently known strategy usually involves an energy-demanding cryogenic process [10,11].

Chemical looping technology is one of the environmentally sound energy conversion processes that can overcome the mentioned challenges. This is because the unique arrangement of a chemical looping unit allows the production of product/flue gas without the presence of nitrogen. The most common setup involves two interconnected fluidized bed reactors where an oxygen carrier is circulated between the two reactors:

namely air and fuel reactors. An oxygen carrier (OC), usually a metal oxide, is oxidized in the air reactor (AR), and then circulated into the fuel reactor (FR), where it is reduced by fuel. The reduced OC is circulated back from the FR to the AR to complete the loop. This enables the fuel to react only with available oxygen carried by the OC without being mixed with any nitrogen.

Another fluidized bed technology which uses oxygen carrier is oxygen carrier aided combustion (OCAC). This is basically a conventional fluidized bed boiler where an oxygen carrier is used as the bed material. This will not directly capture any CO_2, but previous findings demonstrated that the use of an oxygen carrier in OCAC can reduce the emission levels and even enhance the combustion efficiency [12,13]. This implies that OCAC requires less excess air, which makes the carbon capture more favorable.

While chemical looping technology is still in pilot development, OCAC has been operated commercially in several sites in Sweden the recent decade [14]. Figure 1.1 illustrates the basic layout of a chemical looping unit and an OCAC setup.

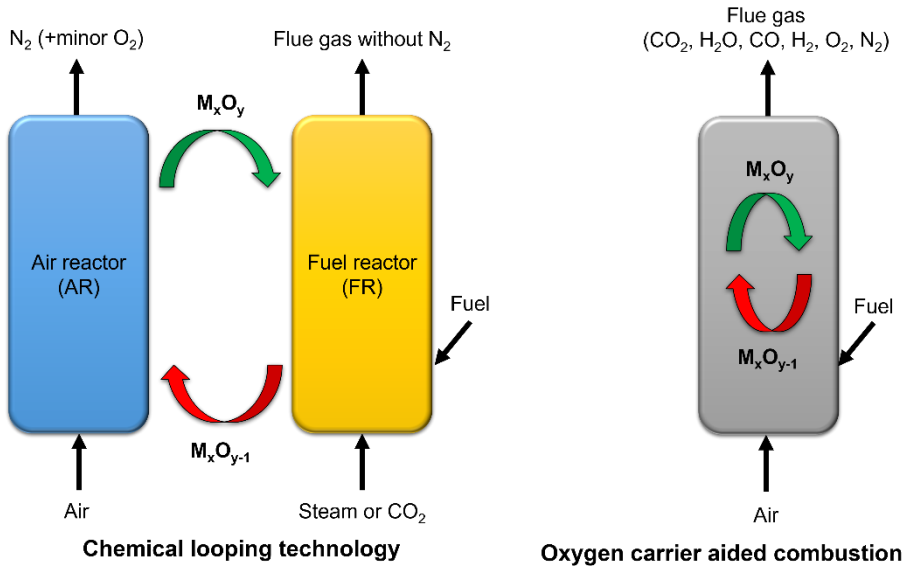

Figure 1.1 Schematic diagrams of a chemical looping unit and an OCAC setup. The green and red curved arrows illustrate a loop comprising oxidized (M_xO_y) and reduced (M_xO_{y-1}) oxygen carriers, respectively. The chemical formulae are only shown as examples and do not necessarily indicate the actual chemical formulae of the oxygen carrier.

Compared to chemical looping technologies, OCAC has a much simpler design and is easier to operate [15]. However, the presence of nitrogen in the flue gas produced in OCAC remains a challenge for removal of the carbon dioxide. Such an obstacle is virtually avoided in chemical looping technology, where nitrogen is kept at bay. Consequently, a carbon capture process does not need to be energy-extensive nor

expensive. A simple condensation can remove the generated steam from the carbon-based flue gases, which subsequently can be compressed and transported to a storage site. If biomass is used as fuel in chemical looping technology, a carbon-negative process is created, which implies reduction of carbon content in the atmosphere.

On the whole, it is not exaggerated to say that a successful operation of both chemical looping technologies and oxygen carrier aided combustion lies on the performance of their oxygen carrier [16]. It is henceforth essential to understand what makes a good oxygen carrier.

1.1.2 Oxygen carrier

An oxygen carrier, at its simplest and the most common form, is a metal oxide with multiple oxidation states. This makes an oxygen carrier able to transfer and release oxygen [17], and as any bed material it can also transfer heat. This is why, as mentioned above, the role of an oxygen carrier is essential in energy conversion processes such as OCAC and chemical looping technology.

A good oxygen carrier should have the following characteristics: sufficiently reactive, highly durable, good fluidization performance, inexpensive, abundantly available, non-toxic and environmentally sound [18]. Certain oxygen carriers have been found to exhibit a unique characteristic known as chemical-looping with oxygen uncoupling (CLOU), where they may release oxygen gas in the fuel reactor [19]. Such an oxygen-releasing property is preferrable, particularly in chemical looping combustion (CLC). Since oxygen is released as gas, it can react much easier with the fuel, allowing for a higher degree of conversion [20].

Many previous studies have investigated the characteristics of various oxygen carriers with different metal oxides [21–23]. Among the most popular ones are iron, manganese, nickel, and copper oxides. At the moment, iron oxides are perceived as promising since they possess most, if not all, of the mentioned desired properties [24–27], not the least its low price and abundant availability.

Obtaining a proper oxygen carrier used to be done through synthesis processes, which adds to the production cost and, henceforth, limits its possible utilization [28]. Nowadays, natural ores such as ilmenite ore seems suitable for many chemical looping applications [18]. Thanks to its reasonable reactivity, easy sourcing, inexpensive cost, and acceptable endurance, ilmenite ore gains popularity as the benchmark oxygen carrier. Low-cost materials open up opportunities for using solid fuels, such as coal and, more preferably and environmentally sound, biomass or waste.

Another attractive alternative to ores can be industrial residues or by-products. The utilization of residue materials as oxygen carriers has both advantages and drawbacks

[29]. From the economic perspective, this can lead to production cost saving since residue materials are often inexpensive and, in their current form, close to worthless, so their potential utilization for energy conversion is obviously desired. Some residue materials have promising properties as oxygen carriers and are produced in quite large amounts. In Sweden alone, 250 – 300 kton of the residue materials iron sand and LD slag are produced annually [14]. Other materials with promising properties are likely generated all around the world in considerable amounts. However, the toxicity level of the residue materials needs to fulfill the safety requirements before it can be processed for oxygen carrier production [30]. In the European Union, strict waste management regulations are already in place [31] regardless of whether the residue materials will be reused or not, so this can facilitate the reutilization of applicable materials as oxygen carriers. Nevertheless, waste materials often perform differently than natural ores due to the way they are generated. For instance, some waste materials have been known to have a lower oxygen transfer capacity than natural ores [32,33]. This is why the investigation of the residue materials continues to eventually yield promising results for utilization in different energy conversion processes.

1.2 Objectives

The aim of the current work is to investigate the behavior of different types of oxygen carriers in conditions relevant for chemical looping processes. More specifically, the stability and reactivity at high degrees of reduction has been explored. Most studies which had been conducted before this work focused on the application of oxygen carriers for combustion-related processes, which aim for complete fuel conversion, such as chemical looping combustion (CLC) and oxygen carrier aided combustion (OCAC). In such cases, only a moderate reduction of the oxygen carriers is expected. Nevertheless, the main application of this work is for processes which require controlling the oxygen transport, such as chemical looping gasification (CLG), chemical looping reforming (CLR), and chemical looping water splitting (CLWS). In these processes, oxygen carriers are expected to get reduced further than in CLC and OCAC by a controlled, and possibly limited, oxidation in the air reactor. Therefore, it is important to evaluate relevant properties as well as performance of oxygen carriers in highly reducing conditions. In this work, the evaluated materials are iron-based materials, which are commonly studied for chemical looping applications and attractive as oxygen carriers due to the advantages mentioned in sub-chapter 1.1.

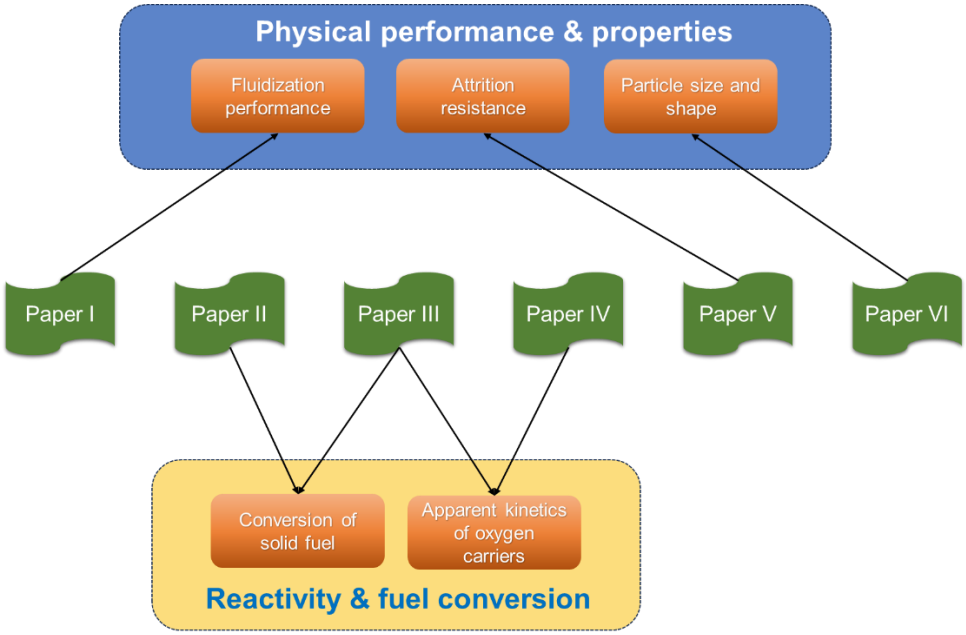

Figure 1.2 Specific objectives of the thesis and correlations with the appended papers.

Figure 1.2 illustrates the specific objects of this thesis and how they correlate with the appended papers. The two main objectives are:

i) assessing physical performance and properties of iron-based oxygen carriers at multiple oxidation degrees, which includes fluidization performance (Paper I), attrition resistance (Paper V), as well as size and shape (Paper VI) of oxygen carriers, and

ii) evaluating reactivity and fuel conversion at multiple oxidation degrees, which covers an apparent kinetic study of oxygen carriers (Paper IV) and evaluation of solid char conversion using oxygen carrier at multiple oxidation degrees (Paper II and Paper III).

2. Oxidation degree of oxygen carriers

2.1 Concept of mass conversion degree

Oxygen carriers perform by transferring oxygen and undergoing redox cycles, making it important to evaluate the oxidation degree of oxygen carriers. A metal oxide M_xO_y undergoes simple reduction and oxidation reactions, which are expected to take place in the fuel and air reactors of a chemical looping unit, according to the following equations [19]:

Reduction: $(2n+m)\ M_xO_y + C_nH_{2m} \rightarrow\ (2n+m)M_xO_{y-1} +\ nCO_2 + mH_2O$ (2.1)

Oxidation: $2M_xO_{y-1} + O_2 \rightarrow\ 2M_xO_y$ (2.2)

By now, it is clear that the metal oxide, which represents oxygen carrier in this case, may lose and regain oxygen through these reactions. This means that the mass, i.e., the weight, of the oxygen carrier may change during the process. This is why mass conversion degree is used as the common basis for expressing the oxidation degree of oxygen carriers in this work.

A fully oxidized oxygen carrier has a mass conversion degree (ω) of 1, or 100 wt.% [34]. In the case of pure iron oxide, this refers to the phase of Fe_2O_3, where iron is at its highest oxidation number: +3. Likewise, any value of mass conversion degree that is lower than 1 indicates that the oxygen carrier is either partially oxidized, e.g., when the oxidation has not been completed, or reduced, which is caused by reducing reaction like fuel conversion. Practically, an oxygen carrier can never have a mass conversion degree of zero since even when the material has lost all its available oxygen, the metallic phase remains. For instance, if one manages to reduce Fe_2O_3 completely to pure metallic iron, the remaining Fe corresponds to a mass conversion degree of 0.7. Furthermore, in some oxygen carriers, there are phases that remain inert during the redox cycles. The inert phases in this case refer to the phases which do not capture nor release oxygen since they are less active than the reacting phases. For example, in the case of iron-titanium oxide (Fe_2TiO_5 in its fully oxidized form), the iron oxide is the active phase which will undergoes oxidation and reduction when exposes in an energy conversion process like OCAC or chemical looping technology, while the titanium oxide (TiO_2) can be perceived as inert which will neither capture nor release oxygen in these conditions.

Figure 2.1 illustrates theoretical correlations between mass conversion degree and crystalline phase transformations during reduction of pure iron oxide (Fe_xO_y). A pure metallic iron phase, which is as far as iron oxide can be reduced, has a mass conversion degree of around 0.7. Note that none of the investigated iron oxygen carriers in this

thesis are 100% iron oxides, so the mass conversion degree values shown in Fig 2.1 are purely illustrative.

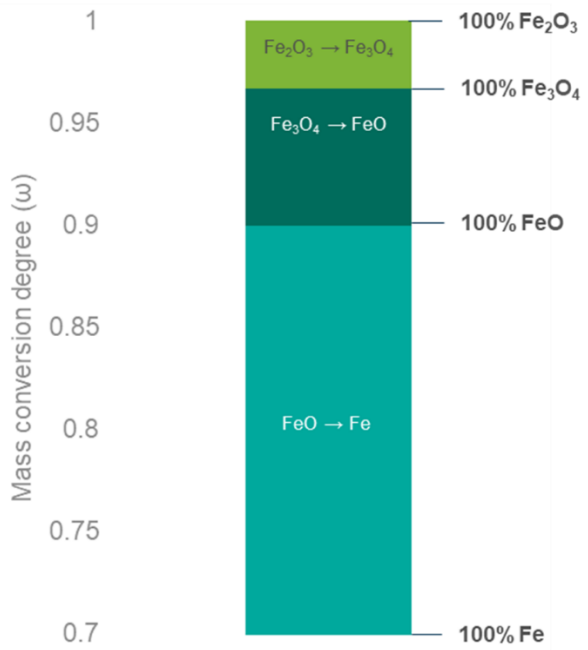

Figure 2.1 Theoretical correlation between mass conversion degree and crystalline phase transformations during reduction of a pure iron oxide (Fe_xO_y).

2.2 Significance of oxidation degrees of oxygen carriers in different processes

When undergoing redox cycles, an oxygen carrier captures and releases oxygen, which subsequently leads to changes in its oxidation number. In chemical looping combustion (CLC) and OCAC, where complete fuel combustion is desired, this usually involves higher mass conversion degrees of Fe-based materials [35]. Suppose this occurs in a pure iron oxide as illustrated in Fig. 2.1, this refers merely to parts of the phase transformation from Fe_2O_3 to Fe_3O_4. For most of the investigated Fe-materials in this study, this usually refers to the mass conversion degrees (ω) between 1 and 0.99. This is why the significance of oxidation degree of oxygen carriers is often overlooked in such processes as it does not raise much concern.

However, this is not necessarily the case with other processes, such as chemical looping gasification (CLG) and chemical looping reforming (CLR), where partial fuel conversion is expected in order to generate valuable products, e.g., syngas [32,36]. In this regard, oxygen transfer from AR to FR has to be controlled to maintain gasification or reforming, instead of complete combustion. There are a few ways to limit oxygen transfer, such as reducing the flow in the AR or diluting the oxidizing gas with inert gas, e.g., nitrogen [37]. This often leads to a partially oxidized oxygen carrier, which will still have to undergo reduction step during fuel gasification in the FR. Understandably, the oxygen carrier may experience a higher degree of reduction compared to CLC or OCAC, thus experiencing a much lower mass conversion degree. A high degree of

reduction in oxygen carrier may lead to potential performance issues, which need to be addressed to establish a successful CLG or CLR operation. In the case of chemical looping water splitting (CLWS), such challenges may even be more pronounced since reductions to FeO or even Fe are expected.

One of the most widely anticipated problems caused by the high reduction degree of an oxygen carrier, i.e., low mass conversion degree, is decreased reactivity. This can have implications for conversions of both gaseous and solid fuels. It is expected that reactivity and oxidation degree of oxygen carriers correlate to a high degree. This makes the evaluation of reactivity at high reduction degrees important in order to optimize the process conditions.

Other important problems that may occur at high degrees of reduction include agglomeration and defluidization of oxygen carriers [38] as well as altered mechanical stability. The latter includes attrition resistance as well as particle size and shape. Compromised attrition resistance and altered particle size and shape have implications for oxygen carriers' lifetime, which may affect the operational cost to some extent. These potential physical performance issues should be considered upon screening and utilization of oxygen carriers. This is why it is essential to correlate the oxidation degree of oxygen carriers with their physical properties and performance.

3. Experimental section

3.1 Materials

3.1.1 Oxygen carriers

All oxygen carriers in this work were pretreated according to the procedure in Fig. 3.1. All materials were naturally obtained ores or by-product-based materials and usually received in suitable size ranges. Still, it was deemed necessary to heat treat and sieve the materials prior to use in order to fully oxidize the material so that there is a common basis for comparison [39]. Afterward, the calcined materials were sieved because the batch reactor works best with a certain particle size range. This step is important to ensure an acceptable fluidization performance. Prior to any experiment, activation of the oxygen carrier bed was performed by exposing the material to several redox cycles, usually between 3 – 10 cycles, using a reactive fuel like syngas or CO at a lower temperature, e.g., 850 or 900 °C. This was done to stabilize the reactivity as well as the structure of the oxygen carriers.

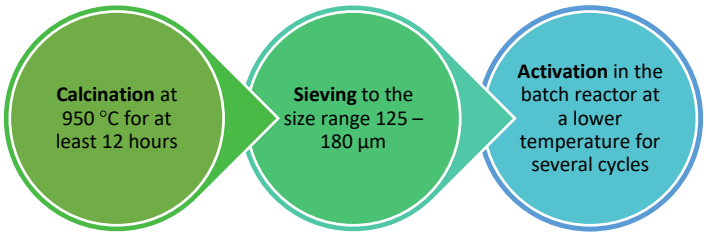

Figure 3.1 General steps in oxygen carrier pretreatment.

Various iron-based oxygen carriers have been investigated. In addition, a couple of manganese-based iron oxygen carriers had also been evaluated with respect to study of defluidization in Paper I, but they are not included in the thesis. Table 3.1 shows the main elemental oxygen-free composition of all the oxygen carriers used in this thesis. It should be noted that the oxygen content, the combustible parts, and the minor constituents are not included in the table. Hence, the figures in the table are normalized values.

Table 3.1 Main elemental composition of oxygen carriers discussed in this thesis.

Element	Composition (wt.%)					
	Ilmenite	Iron sand	LD slag	Tierga ore	Synthetic ilmenite	Mill scale
Fe	54	65	29.3	90.4	54	95
Mn	0.7	0.6	4.5	0.1	-	1.0
Ti	45	0.2	1.3	0.1	46	-
Si	0.2	30	9.7	5.9	-	4.0
Ca	0.1	4.2	55.2	3.5	-	-

3.1.2 Gases

The gases used in this work are common gases that are present in most combustion or gasification processes. Furthermore, they make up common constituents of biomass volatile matters [40]. Table 3.2 provides a summary of gases used in this thesis. Syngas, methane, hydrogen, and carbon monoxide are reducing gases and considered as gaseous fuels. The oxygen content in the oxidizing gas was limited to 5 vol.%, instead of around 21 vol.% in normal air, since this is the target oxygen concentration in the outgoing gas at the top of the riser of a chemical-looping combustion unit [41,42]. Using this concentration is reasonable given that an oxygen carrier should be able to be oxidized at lower partial pressures of oxygen than that of air in order to be deemed feasible for utilization. Additionally, using a low concentration of oxygen is practical to avoid excessive heating during the exothermic oxidation step [43].

Table 3.2 Gases used in this thesis.

Gases	Composition
Oxidizing gas	5% O_2 in N_2
Nitrogen	100% N_2
Syngas	50% CO in H_2
Methane	100% CH_4
Hydrogen	100% H_2
Carbon monoxide	100% CO
Diluted CO	50% CO, 50% N_2

3.1.3 Solid fuel

In this thesis, there was only one solid fuel used, namely pine forest residue char. The fuel was obtained from Navarra, Northern Spain [44]. The char was prepared according to the scheme in Fig. 3.2 prior to being exposed to the solid fuel reactivity tests. Using raw fuel directly in the experiments was deemed not feasible as the material in its original form tends to stick to the inner surface of the feeding line.

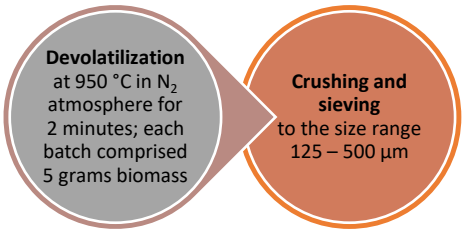

Figure 3.2 Steps in solid fuel preparation.

Devolatilization is considered an important step with an aim to remove the major volatile contents in the char [45]. In this way, the obtained char conversion rate can be correctly interpreted as the char gasification rate and the influence from reaction with volatile matters should be negligible and disregarded. Even though both volatile and char conversions are relevant to applications in a chemical looping unit, the focus here is to evaluate the latter.

Crushing and sieving were necessary to acquire a suitable size range of solid fuel; otherwise, the fuel feeding into the batch reactor would have been challenging. Were the char obtained as fine matters, it would likely stick to the inner surface of the feeder and, thus, not get into the reactor. The other possibility is that the char would just leave with the gas flow before reacting with the bed. On the other hand, if the fuel is too coarse, it might get stuck within the feeders and block the char feeding system. In the experiment using solid fuel, nitrogen and steam were also present in the bed to facilitate the fluidization and gasification, respectively. The composition of pine forest residue char can be found in both Paper II and III.

3.2 Equipment

3.2.1 Fluidized bed batch reactor setup

Most of the work done in this thesis involved experiments in a batch fluidized bed reactor. The fluidized bed batch reactor setup is illustrated in Fig. 3.3 below. In this context, batch means that the operation is non-continuous; thus, a series of steps is involved. The weight of the oxygen carrier bed is usually between 15 and 20 grams. Using the batch reactor setup makes it possible to evaluate the properties and behavior of oxygen carriers with controlled parameters. For instance, the oxidation degree of oxygen carriers can be controlled by setting a certain reduction time. It is also possible to mimic certain conditions of a chemical looping process in this unit, e.g., reduction step in the batch reactor should be able to mimic relevant conditions in a fuel reactor. Moreover, the small size of the setup ensures homogeneous conditions over the oxygen carrier bed, which is not the case in a larger unit. Nevertheless, the small size of the

setup means that it is not possible to perform a direct physical upscaling to the large-scale unit due to the much lower fluidizing velocity. The details of this setup has been reported previously [46].

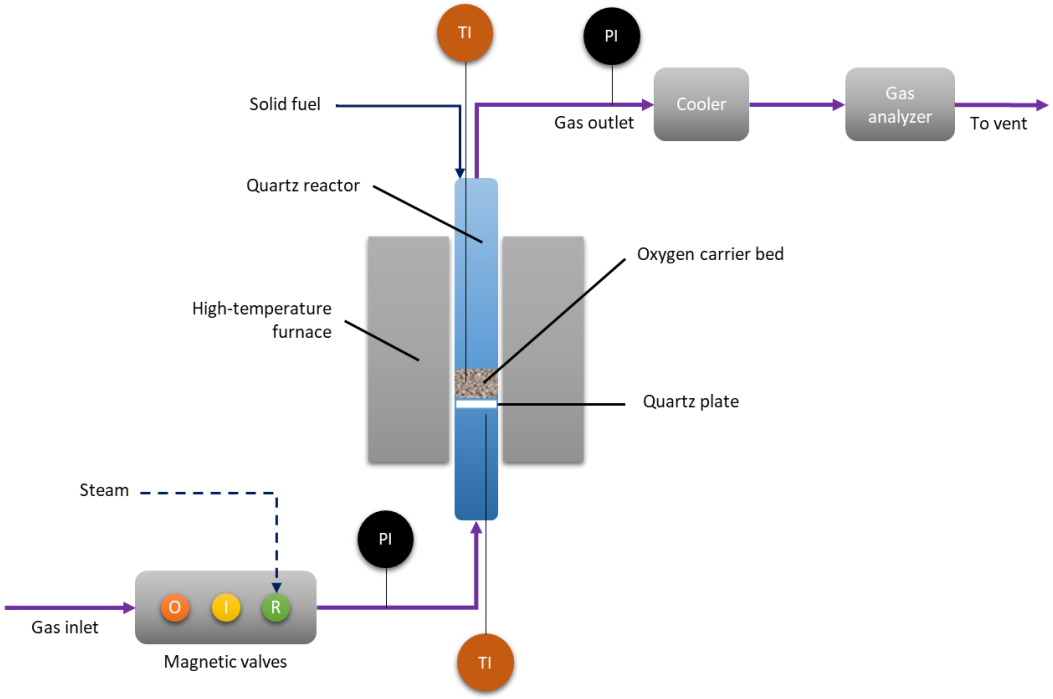

Figure 3.3 Schematic diagram of the fluidized bed batch reactor setup.

The same setup was used for experiments using both solid and gaseous fuels. However, the ways to feed the fuel differs. The feeding of different gases is regulated by three magnetic valves and the gas will enter the reactor from the bottom end. The reducing flow may also include steam in the case of solid fuel conversion. O, I, and R indicate oxidizing, inert, and reducing gases, respectively, see sub-section 3.3.1 for more details. Steam is generated by a controlled evaporator mixer Bronkhorst type W-202A-300-K. Meanwhile, solid fuel is fed into the reactor from the top with the help of nitrogen as sweep gas to ensure the solid fuel encounters the oxygen carrier bed. Normally, the sweep gas does not reach the particle bed due to its relatively low velocity, which was set no more than half of the fluidizing gas velocity, therefore does not affect the fuel conversion in the bed itself. In this thesis, the ratio of fluidization velocity (U) to the respective minimum fluidization velocity (U_{mf}), symbolized as U/U_{mf}, usually ranges from 1.7 to 3.3 depending on the fluidizing gases.

The height and inner diameter of the quartz glass reactor are 820 mm and 22 mm, respectively. The oxygen carrier bed particles are placed on top of a porous circle-shaped quartz plate, which was located 370 mm above the reactor's bottom edge. The reactor was placed in a high-temperature furnace manufactured by ElectroHeat Sweden AB, with a maximum temperature of 1,400 °C. The inlet and outlet of the reactor were

equipped with Swagelock® tight-sealed connections to avoid gas leakage. Heating tape was wrapped around the top and bottom parts of the reactor, i.e., the area located outside the furnace, to avoid the condensation of gas, particularly water vapor. The temperature inside the bed of particles was measured using a type-K thermocouple that was placed in a quartz cover, indicated by TI. The pressure monitoring, indicated by PI, is done by using a 20-Hz Honeywell pressure transducer (more details in the next paragraph). The outlet gases were cooled down by an M&C ECP1000 cooler before entering the analyzer; thereby removing the water contents. A Rosemount™ NGA 2000 gas analyzer measured the real-time gas volumetric flow rates and concentration of CO, CO_2, CH_4, H_2, and O_2.

The pressure monitoring setup, which is particularly relevant for monitoring the fluidization of the particle bed (sub-section 4.1.1 and Paper I), is elaborated below. For this purpose, a 20-Hz Honeywell pressure transducer was employed to measure the pressure difference between the inlet and outlet of the reactor. Despite its small frequency, the pressure transducer works sufficiently well to judge the bed fluidization in the small batch setup. When defluidization occurs, the pressure amplitude drops significantly in the pressure monitor. This is illustrated in Fig. 3.4.

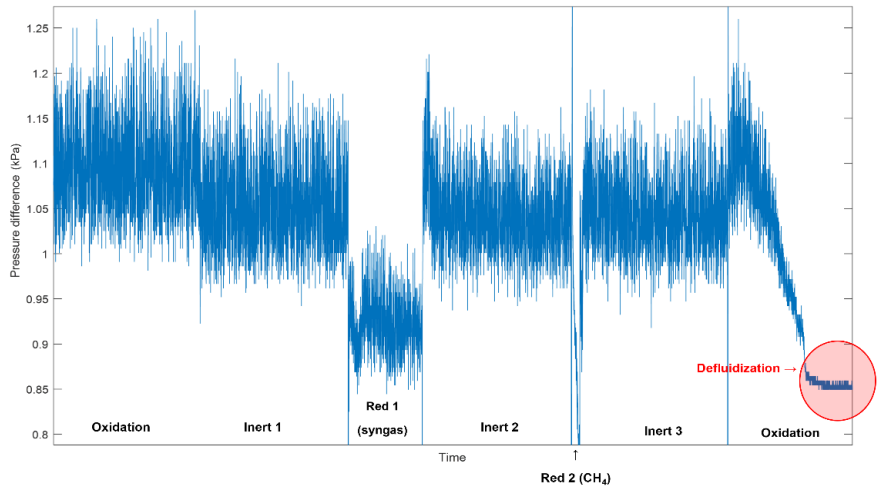

Figure 3.4 Defluidization detected in the bed based on the sudden decrease in pressure fluctuations during oxidation. In this case, the oxygen carrier ilmenite was examined at 900 °C, and defluidization happened during the oxidation step that followed a 90-second syngas reduction, which corresponds to a mass conversion degree (ω) of around 0.97. The frequency of pressure measurement was 20 Hz.

In Fig. 3.4, the bed defluidization is indicated by a change in the pressure fluctuation, which suddenly drops. However, not all sudden drops in the pressure fluctuations indicate a defluidized bed. For example, the sudden drop between oxidation and inert 1 or between inert 1 and reduction 1 in the graph was due to different flow rates and

changes in flow streams. A simple test in cold conditions suggested that the particle bed can still be deemed fluidizing when the standard deviation (SD) of pressure fluctuations is higher than 0.02 kPa. The SD usually ranges from 0.03 to 0.06 kPa during the whole experiment in hot conditions when the bed is fluidized. Note that the SD value is simply used to judge the fluidization state of the bed based on pressure fluctuations and does not necessarily indicate the absolute pressure in the bed.

3.2.2 Customized jet cup rig

A customized jet cup rig, illustrated in Fig. 3.5, was used to examine the attrition rate of oxygen carriers prepared in the fluidized bed batch reactor (sub-section 4.1.2 and Paper V). The physical conditions in the batch reactor in themselves are not sufficient to trigger measurable attrition phenomena due to the low fluidization velocity and minimal wall effects [46]. However, relevant chemical conditions, e.g., the oxidation states in this case, can be set properly in the fluidized bed [46]. A jet cup device is commonly used for evaluating the attrition rate of particles, but the device cannot consider the thermal and chemical influences. There is an available ASTM standardized method for evaluation in the jet cup device [47], but this typically requires considerable amount of samples (about 65 grams). Due to the limited amount of oxygen carrier samples obtained in this study (15 – 20 grams), a customized jet cup device is more applicable for attrition examination [48]. The rig of the customized device allows the gas inlet to flow in a tangential flow, mimicking particle-wall collisions (mechanical stress) in cyclones, fluidized bed, and risers [49]. In this way, it is possible to correlate the degree of oxidation set in the batch reactor with the attrition rate measured in the customized jet cup device.

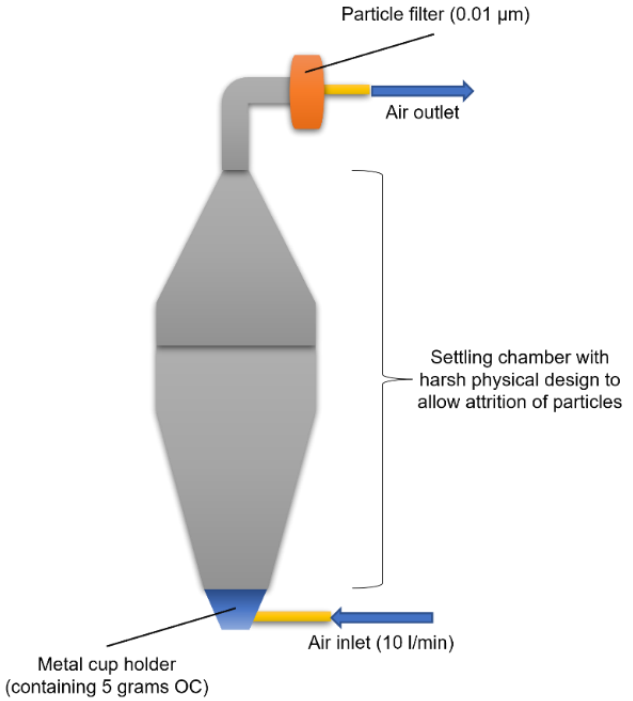

Figure 3.5 Schematic diagram of the customized jet cup rig device.

Five grams of an oxygen carrier sample are put into the metal cup holder at the bottom of the rig. A flow of ten liters per minute of air (25 °C, 1 atm) was first flown into a humidifier containing a 25-cm water column. This was done to minimize the risk for static electricity in the settling chamber, which lead to particles sticking to the chamber wall. The humidified air flow was then fed into the jet cup rig from the inlet nozzle (inner diameter = 1.5 mm) placed tangentially at the bottom of the cup holder. This air flow creates an upward particle vortex throughout the cup and eventually into the settling chamber. The oxygen carrier particles will experience mechanical stress during this process due to the high air velocity and harsh physical environment inside the apparatus. Eventually, heavier particles with generally larger sizes will fall back into the cup, while the generated fines will be carried toward the outlet and trapped by a 0.01 micron-filter. The filter is weighed every 10 minutes for an hour in order to estimate the attrition resistance of the particles. At the end of the experiment, both samples left in the cup holder and trapped in the filter can be collected for further analysis.

3.2.3 Particle size analyzer

This equipment is located at the Division of Energy Engineering, Luleå University of Technology. The device was used to analyze the size and shape of oxygen carrier particles after exposure in the fluidized bed batch reactor (sub-section 4.1.3 and Paper VI). The particle size analyzer of Camsizer XT manufactured by Retsch GmbH is able to investigate powders and granules in a size range from 1 micron to 3 millimeters with dynamic image analysis (DIA). The particles are fed from a hopper by vibration and transported by a chute into the field of view. The gravity dispersion (X-fall) method was chosen to disperse the particles as sample recovery is possible with this technique. Here, the dispersed particles passed through a pair of LED light sources, which have different angles. The created shadows were subsequently captured by two high resolution cameras – one being responsible for small particles (zoom camera) while the other for the large particles (basic camera). These shadowgraph images are then processed for particle size and shape analysis by the Camsizer XT software (version 6.9.66.1206, Microtrac Retsch GmbH). This procedure was repeated 2 – 3 times for each oxygen carrier using at least 7 – 8 grams sample. In case of limited amount, the repetition was performed using the same batch of samples. Samples were divided homogeneously with a rotary divider (Retsch Technology). Over one million particles were detected by the software.

3.3 Experimental methods

The methodology for the experiments varied depending upon the goal and aim of the particular study; for details, see the appended papers.

3.3.1 General steps in a cycle in the batch fluidized bed reactor

A cycle in the fluidized bed batch experiment has three main steps. This is illustrated in Fig. 3.6.

Figure 3.6 Three steps in a cycle in the fluidized bed batch reactor experiment.

Normally, a cycle starts with oxidation, where the oxygen carrier is oxidized with 5% O_2 in N_2, and then followed by an inert period, where nitrogen is used to purge the remaining oxygen in the system. During the reduction, either steam or gaseous fuel is injected into the bed. Steam is mainly used for solid fuel experiments, where solid fuel is dropped from the top via a two-way valve. After the reduction, another inert period will follow to purge the remaining flue gases. The next step can be either oxidation, which marks the beginning of a new cycle, or another reduction step, depending on the experimental plan. For example, several experiments in this thesis involved two steps of reduction in a single cycle. In such cases, the sequence in a cycle was oxidation – inert – reduction 1 – inert – reduction 2 – inert. In some cases, the reduction comprises several short pulses with inert phases in between each pulse, like in the case with Papers III and IV. The specific method for each article can be found in the appended papers.

3.3.2 Attrition rate investigation and particle size and shape analysis

The attrition rate of oxygen carriers was investigated in Paper V, while their particle size and shape were analyzed and discussed in Paper VI. Twenty grams oxygen carrier was prepared in a fluidized bed for several cycles (refer to sub-section 3.3.1) producing samples at different reduction degrees. A part of each sample was examined in the jet cup rig (see sub-section 3.2.2), while the rest were sent to the particle size and shape analysis in Luleå University of Technology (see sub-section 3.2.3). The procedure is summarized in Fig. 3.7.

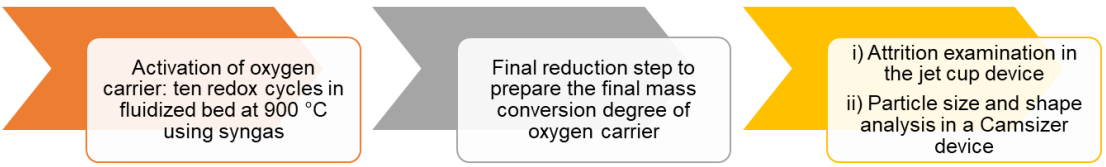

Figure 3.7 Summary of procedure for attrition rate investigation and particle size and shape analysis.

3.4 Oxygen carrier characterization

There are several characterization techniques performed in this thesis.

i) Crystalline phases

The crystalline phases of oxygen carrier samples were analyzed using XRD Bruker D8 Advance or Discover. The analysis took roughly an hour for each sample with at least 800 steps using a copper or molybdenum radiation source – the latter applies to sub-sections 4.1.2 and 4.1.3, which corresponds to Paper V and VI, respectively. This was done to see how the phases of oxygen carriers might have transformed during the experiment. In some cases, like the one portrayed in sub-section 4.1.2 (Paper V), a semi-quantitative (S-Q) analysis result was also calculated from XRD diffractograms.

ii) Sample topography

The surface morphology and elemental distribution in the oxygen carrier were analyzed using SEM/EDX JEOL 7800F Prime in most cases, or Phenom ProX and FEI ESEM Quanta 20 in the works discussed in sub-section 4.1.2 (Paper V), using a backscattered electron detector with an acceleration voltage between 10 to 15 kV. The oxygen carrier particles were embedded in epoxy and polished to provide a cross-sectional view under EDX. From this analysis, it is possible to visualize the structural changes that the oxygen carriers had undergone during experiments. In the case of specific defluidization tendency examination in Paper I and sub-section 4.1.1, the defluidized oxygen carriers were observed under the light microscope Nikon SMZ800 to see how the particles looked like after the experiments, e.g., how agglomerated particles were attached to each other. With respect to Paper III, the BET surface area of iron sand has been measured using Micromeritics TriStar 3000.

3.5 Data evaluation

3.5.1 Gaseous fuel experiments

The mass conversion degree ω of the oxygen carrier under reduction with several gaseous fuels is calculated based on equations listed in Table 3.3. Here, x, $\dot{n}$, and M_O indicate mol fraction, molar gas flow, and molecular weight of oxygen (16 g/mol), respectively.

Table 3.3 Formula to calculate the mass conversion degree of the oxygen carrier upon reduction by various gaseous fuels.

Gaseous fuel	Formula to calculate mass conversion degree	Equation number
Syngas (50% CO in H_2)	$\omega = \omega_0 - \int_{t_0}^{t} \frac{\dot{n}\, M_O}{m_{ox}} \left(2x_{CO_2} + x_{CO} - x_{H_2}\right)dt$	(3.1)
Methane	$\omega = \omega_0 - \int_{t_0}^{t} \frac{\dot{n}\, M_O}{m_{ox}} \left(4x_{CO_2} + 3x_{CO} - x_{H_2}\right)dt$	(3.2)
CO	$\omega = \omega_0 - \int_{t_0}^{t} \frac{\dot{n}\, M_O}{m_{ox}} \left(x_{CO_2}\right)dt$	(3.3)
H_2	$\omega = \omega_0 - \frac{M_O}{m_{ox}} \int_{t_0}^{t} \left(\dot{n}_{H_2,in} - \dot{n}_{H_2,out}\right) dt$	(3.4)

The yield of a carbon-based gas species *i* (γ_i) was defined as the mol fraction of gas species *i* divided by the total mol fraction of the carbon-based gases measured in the outlet. These include CO_2, CO, and CH_4, as they are the only three gases that the gas analyzers can possibly detect.

$$\gamma_i = \frac{x_i}{x_{CO_2} + x_{CO} + x_{CH_4}} \tag{3.5}$$

In this thesis, the conversion rate for gaseous fuel *i*, symbolized as r_i, was defined as the change of mass conversion degree within a certain period.

$$r_i = \frac{-d\omega}{dt} \tag{3.6}$$

3.5.2 Solid fuel conversion

In regards to sub-section 4.2.2 (Paper II and III), the fraction of converted carbon, X_c, was defined as the total carbon released during a specific time divided by the total carbon emitted from the converted char, $m_{c,total}$, during the conversion period.

$$X_c = \frac{M_c \int_{t_0}^{t} \dot{n}\,(t)\left(X_{CO}(t) + x_{CO_2}(t) + x_{CH_4}(t)\right)dt}{m_{c,total}} \tag{3.7}$$

Meanwhile, the conversion rate of char, symbolized as r_c, was defined as a function of X_c as shown in the formula below.

$$r_c = \frac{dX_c}{(1 - X_c)\, dt} \tag{3.8}$$

It should be noted that the solid fuel conversion rate in this work was calculated within the range $0.3 < X_c < 0.7$, as this has been deemed the suitable range where the conversion rates are more stable based on previous tests in the same setup [50]. At a fraction of converted carbon lower than 0.3, the conversion rate may have an overshot due to the volatile release in the beginning of the char conversion. As mentioned in sub-chapter 2.2, both reactions with gaseous and solid fuels can take place in a chemical looping unit, but in this regard the focus is to evaluate the char conversion. This is why the influence from reactions with volatile matters needs to be disregarded in this specific case. On the other hand, the rate observed in $X_c > 0.7$ may be overestimated due to the very low amount of fuel in the bed combined with low outlet flue gas concentration. To be specific, the denominator in Eq. 3.8 becomes very low and the rate calculation will therefore be unreliable.

3.5.3 Attrition rate and particle size and shape analysis of oxygen carrier

With respect to attrition resistance examination in sub-section 4.1.2 (Paper V), the attrition rate of an oxygen carrier can be quantified by the attrition rate A (in wt.%/h), which is defined as the amount of generated fines divided by mass of the initial bulk sample (about 5 grams) collected over a certain time, i.e., 10 minutes for each increment.

$$A = \frac{mass\ of\ collected\ fines\ (g)}{mass\ of\ bulk\ sample\ (g) \times observation\ time\ (h)} \times 100\% \quad (3.9)$$

In the light of particle size and shape analysis discussed in sub-section 4.1.3 (Paper VI), the size distribution can be characterized by different dimensions, such as equivalent particle diameter, particle width, and length. In this work, the particle width was selected to characterize the particle dimension due to the good agreement with the sieving method. The particle width, $x_{c,min}$, is defined as the narrowest distance between two points on the particle edges among all the measured chords, perpendicular to the scanning direction. The opposite of this, i.e., the longest distance, is called the particle length, $x_{Fe,max}$, which is determined from the longest of all measured Feret diameters (maximum distance between two parallel tangents). Figure 3.8 illustrates these measurements in a single particle.

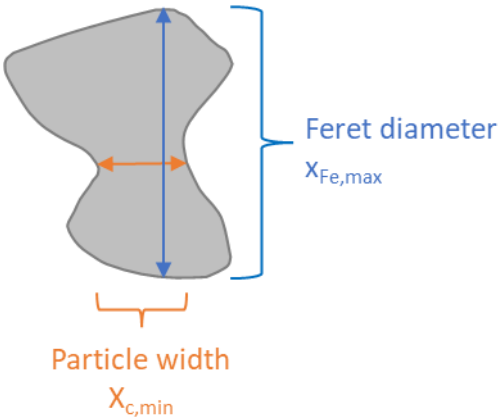

Figure 3.8 Illustrations of particle width and Feret diameter in a single particle.

Sphericity is the ratio of the perimeter of the equivalent circle P_s (based on the same surface area, A) to the actual perimeter P of the particle. This can be further expressed as follows.

$$\text{Sphericity} = \frac{P_s}{P} = \frac{\sqrt{4\pi A}}{P} \quad (3.10)$$

The aspect ratio of a particle is defined as the ratio between its width to its length.

$$\text{Aspect ratio} = \frac{x_{c,min}}{x_{Fe,max}} \quad (3.11)$$

3.6 Reactivity models

3.6.1 Apparent kinetic model fittings of oxygen carrier reactivity in gaseous fuel conversion

This part concerns Paper IV and sub-section 4.2.1. The aim is to assess the effect of temperature (T), mass conversion degree (ω), and molar gas concentration of reactants around the oxygen carrier particles (C_g) on oxygen carrier reactivity during conversions of gaseous fuels. Since most of the published studies used the degree of solid conversion α, which represents the conversion degree of active oxygen, to correlate the solid conversion with the reactivity, there is a need to convert mass-based conversion degree $\omega \in [1,0]$ to $\alpha \in [0,1]$ due to the different domains. This means that α indirectly represents ω. This can be expressed by the following [51]:

$$\alpha = \frac{1-\omega}{R_O} \quad (3.12)$$

The reactivity of oxygen carrier can, therefore, be expressed as follows [52].

$$r_i = \left(\frac{d\alpha}{dt}\right)_i = f(\alpha) \times h(C_g) \times k(T) \quad (3.13)$$

By using the model-fitting method, the following steps were performed in the apparent kinetic study.

i) First, under isothermal conditions, *f(α)* can be integrated to *g(α)* by applying this formula:

$$g(\alpha) = \int_{\alpha_0}^{\alpha_t} \frac{d\alpha}{f(\alpha)} = h(C_g) \times k(T)t \quad (3.14)$$

Therefore, we get a series of *g(α)* values for each temperature. The experimental data can therefore be fitted to Eq. 3.14 using different available transparent models, which can be found in Paper IV. The slope, *dg(α)/dt*, would then be the product of $h(C_g) \times k(T)$. Note that the value of $h(C_g)$ and *k(T)* are relatively constant in this study, so *g(α)* only changes with time. See point (ii) and (iii) for more information.

The quality of the solid conversion model, that is, Eq. 3.14, is determined by three factors:

a) Pearson correlation coefficient (R^2), which shows how linear a model fitting is.

$$R^2 = \frac{\left(n\sum ty_j - \sum t_j \sum g(\alpha)_j\right)^2}{n^2\left(\sum t_j^2 - \left(\sum t_j\right)^2\right)\left(\sum g(\alpha)_j^2 - \left(\sum g(\alpha)_j\right)^2\right)} \quad (3.15)$$

where n = data matrix size and j = data index.

This correlation coefficient may vary at different temperatures, but the common basis for comparison in this work is the average value of R^2 obtained at different temperatures.

b) Analysis on a plot of reactivity r_i (Eq. 3.15) vs ω. In this step, it should be determined whether the reactivity trend is physically reasonable or not. This is because a high R^2 value does not necessarily correspond to a reasonable physical model.

c) Assessment on how close the model-predicted value is to the experimental value.

ii) The next step is to obtain the rate constant *k(T)* for each model from the obtained slope (Eq. 3.13). Since the slope is a product of *k(T)* and $h(C_g)$, the latter must be determined first. In this study, $h(C_g)$ corresponds to the molar reactant gas concentration surrounding the oxygen carrier particles. Even though the inlet gas concentration was not varied for any gaseous fuel, the gas concentration around the particle might vary and have an influence on reactivity of the oxygen carriers. Therefore, the effect of the molar gas concentration needs to be assessed as well. Assuming a first-order reaction, the boundary molar gas concentration was estimated as the logarithmic mean ($\overline{C_g}$) between inlet and outlet molar reactant gas concentrations. The driving force of molar gas concentration around the particles for each pulse can therefore be formulated as:

$$h(C_g) = \overline{C_g} - C_{eq} = \frac{C_{g,inlet} - C_{g,outlet}}{ln\frac{C_{g,inlet}}{C_{g,outlet}}} - C_{eq} \quad (3.16)$$

where C_{eq} is the gas concentration around the particles at equilibrium.

In this study, however, it was later found that $h(C_g)$ does not change substantially, even at different temperatures. This suggests that a significant variation in gas concentrations cannot be reached without varying inlet gas concentrations in the batch reactor. Therefore, the $h(C_g)$ value considered in this study is the average of all the obtained

$h(C_g)$ values at one single temperature. Hence, the $h(C_g)$ value is considered to be constant for each temperature.

The value of the rate constant for each temperature, $k(T)$, can thereafter be determined by dividing the slope obtained from Eq. 3.14 with $h(C_g)$ from Eq. 3.16. Note that $dg(\alpha)/dt$ in Eq. 3.17 merely symbolizes the slope value obtained from Eq. 14 for each temperature and does not suggest any influence of α on $k(T)$. Since both $dg(\alpha)/dt$ and $h(C_g)$ are constant for each temperature, this will result in a constant $k(T)$ for each temperature as well.

$$k(T) = \frac{\frac{dg(\alpha)}{dt}}{h(C_g)} \tag{3.17}$$

iii) The obtained rate constant was then plotted against the respective temperature according to the Arrhenius equation,

$$k(T) = k_0 e^{\frac{-E_a}{RT}} \tag{3.18}$$

where k_0 = pre-exponential factor, E_a = activation energy, and R = universal gas constant.

By taking the logarithmic of the Arrhenius equation (Eq. 3.18),

$$ln\, k(T) = ln\, k_0 + \left(\frac{-E_a}{R}\right)\frac{1}{T} \tag{3.19}$$

3.6.2 Char reactivity models

The char reactivity in a fluidized bed batch reactor using two different oxygen carriers, ilmenite and iron sand, was investigated and compared in this thesis. The kinetic parameters k_0 and E_a can be obtained using Eqs. 3.18 and 3.19. In this case, however, r_i is replaced with r_c, to clarify that the context is char conversion.

It is important to stress that the oxygen carrier itself does not have any direct reaction with the char in a fluidized bed. Instead, the char is converted (or gasified, in this case) by CO_2 or H_2O in the gas phase around the char particles [53]. In a common setup of chemical looping unit, this takes place in the fuel reactor. The char conversion rate can be suppressed by the presence of both hydrogen and carbon monoxide [54]. In steam char conversion, the inhibition effect caused by hydrogen partial pressure has been found to be more important than that of carbon monoxide, which is usually more relevant for CO_2 gasification [50]. A high concentration of hydrogen has been found to significantly suppress the char conversion rate [55]. The proposed main mechanisms taking place in a steam char conversion are summarized in Table 3.4. These mechanisms have been previously found to be suitable to interpret steam char conversion, where a mixture of steam, CO, CO_2, and CH_4 is involved [54,56]. C_f represents a free active site on the char's

surface and $C(X)_n$ denotes a char's surface complex which adsorbs n molecules of species *X*.

Table 3.4 The Langmuir – Hinshelwood mechanisms which have been explored in this thesis.

Mechanism	Reaction	Inhibition occurrence
Oxygen exchange (OE)	$C_f + H_2O \underset{k_{-1}}{\overset{k_1}{\rightleftharpoons}} C(O) + H_2$ $C(O) \overset{k_2}{\rightarrow} CO + C_f$	If more hydrogen is added, the formation of C(O) may be suppressed.
Associative hydrogen adsorption (AHA)	$C_f + H_2 \underset{k_{-3}}{\overset{k_3}{\rightleftharpoons}} C(H)_2$	The added hydrogen is adsorbed directly onto the active sites from the gas phases.
Dissociative hydrogen adsorption (DHA)	$C_f + \frac{1}{2}H_2 \underset{k_{-4}}{\overset{k_4}{\rightleftharpoons}} C(H)$	

The hydrogen inhibition mechanisms can be translated into three conversion rate models, which are all based on the general surface rate equation below, known as the Langmuir – Hinshelwood rate expression [56].

$$r_c = \frac{ck_1 p_{H_2O}}{1+\frac{k_1}{k_2}p_{H_2O}+f(p_{H_2})} \tag{3.20}$$

where r_c = solid fuel conversion rate, p_{H_2O} = steam partial pressure, and p_{H_2} = hydrogen partial pressure.

The three proposed Langmuir-Hinshelwood mechanisms taking place in a steam char conversion were mainly based on the hydrogen inhibition effect and can be found in Paper II.

4. Results and discussion

With respect to high degrees of reduction of oxygen carriers, the main parts in this thesis are physical performance and properties, as well as reactivity and fuel conversion. Investigating the physical performance and properties of oxygen carriers is essential for material screening as well as predicting materials' behaviors and lifetime. To be specific, this includes investigation of fluidization performance, which is also crucial for reactor design, and evaluation of attrition rate and particle size and shape, both being indicators for material stability. On the other hand, assessing reactivity of material is useful for both material screening and engineering design, e.g., determination of the amount of oxygen carrier bed and circulation rate in a chemical looping unit. In addition, fuel conversion rate needs to be considered when designing the fuel reactor so that an optimum fuel feeding rate can be established. Figure 4.1 illustrates how each part of the thesis contributes to these applications.

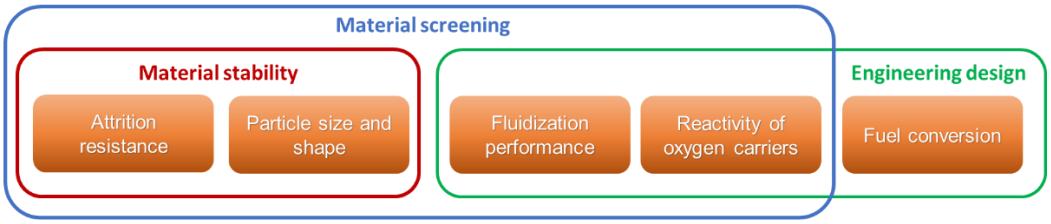

Figure 4.1 How parts of this thesis contribute to applications in chemical looping processes.

4.1 Physical performance and properties of oxygen carriers

In the light of deep reduction of oxygen carriers, the physical performance and properties of oxygen carrier is investigated from different perspectives: fluidization performance, attrition resistance, and shape and size analysis.

4.1.1 Fluidization performance

It was hypothesized that a highly reduced oxygen carrier may experience fluidization issues caused by particle agglomeration and defluidization. The aim of this part is to gauge the defluidization tendency of various iron-based materials at high degrees of reduction. All the investigation was conducted in a fluidized bed batch reactor at 900 °C with a U/U_{mf} ratio between 2.2 and 3.0 under reduction with syngas. The pressure fluctuation was monitored to determine if the bed was fluidized or not, see sub-section 3.2.1 and Paper I for experimental details. The summary of the results is provided in Table 4.1 below. The after-used materials were obtained from operations in a 300-W chemical looping unit for 7 – 12 hours [57].

Table 4.1 Defluidization occurrence of various iron-based oxygen carriers in a fluidized bed batch reactor.

Oxygen carrier			Stage when defluidization occurred	Mass conversion degree (ω)*
Name	State	Abbreviation		
Ilmenite ore	Freshly calcined	ILFC	Oxidation	0.968
	After-used	ILAU	Oxidation	0.961
Tierga ore	Freshly calcined	TOFC	Oxidation	0.960
LD slag	Freshly calcined	LDFC	Never occurred	-
	After-used	LDAU	Never occurred	-

*The value of mass conversion degree was obtained from the last reduction step, i.e., before defluidization occurred in the following oxidation.

The results show that both ilmenite and Tierga ores defluidized at high degrees of reduction, and the defluidization took place during the oxidation period that follows the longest reduction period. Both freshly calcined and after-used LD slag did not defluidize even though they had been reduced to a mass conversion degree of around 0.986, where conversion of CO to CO_2 was no longer observed. The most likely explanation is that this material has a rather low iron content compared to the other iron-based oxygen carriers, see Table 3.1.

The crystalline phases of the defluidized oxygen carriers are provided in Table 4.2 and an example of the XRD diffractograms is provided in Fig. 4.2; the rest can be seen in Paper I. The names of the detected phases are also shown in Fig. 4.2. All the activated materials, that is, materials obtained from the experiments in the fluidized bed batch reactor, were in a reduced condition when they were analyzed with XRD.

Table 4.2 The main phases in the oxygen carriers that defluidized at various mass conversion degrees confirmed by XRD.

Sample	Mass conversion degree	Detected crystalline phase
ILFC	1.000 (freshly calcined)	Fe_2O_3, Fe_2TiO_5
	0.989	Fe_2TiO_5
	0.978	Fe_2O_3, Fe_3O_4
	0.968 (defluidized)	Fe_3O_4, $FeTiO_3$, FeO, Fe
ILAU	After-used, as received	Fe_2O_3, Fe_3O_4
	0.986	Fe_2TiO_5, Fe_3O_4
	0.975	Fe_2TiO_5, Fe_3O_4, FeO
	0.961 (defluidized)	FeO, Fe
TOFC	1.000 (freshly calcined)	Fe_2O_3
	0.990	Fe_2O_3, Fe_3O_4
	0.971	Fe_3O_4, FeO
	0.960 (defluidized)	Fe_3O_4, FeO, Fe

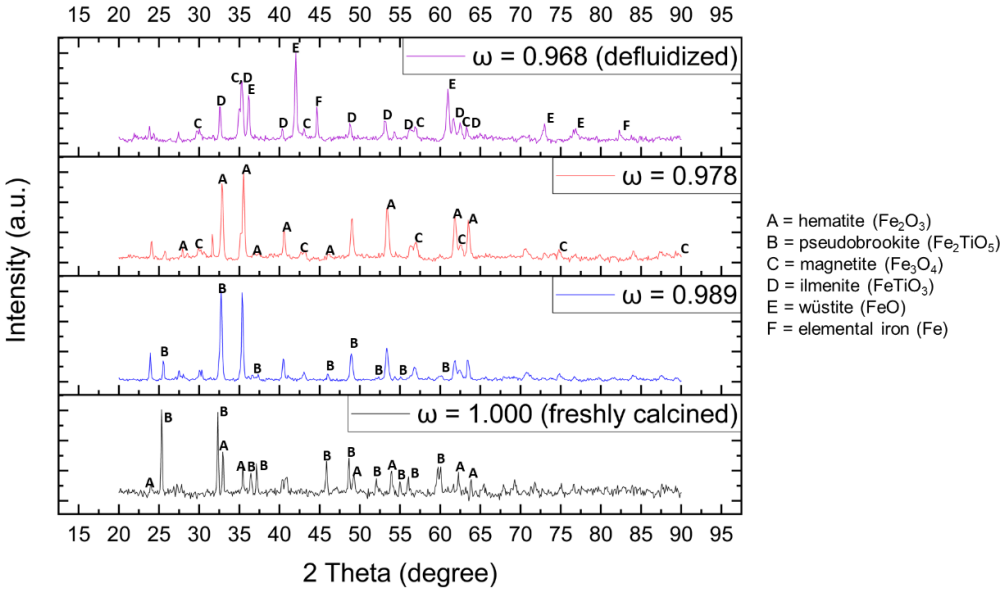

Figure 4.2 Example of diffractograms of the defluidized oxygen carriers, i.e., freshly calcined ilmenite ore (ILFC) in this case, at various mass conversion degrees.

Based on the results, the defluidization occurrence was likely attributed to the formation of highly reduced iron oxide phases, such as wüstite (FeO) and elemental iron (Fe), and iron migration to the outer surface of the particle. The latter is a common phenomenon during reduction of iron oxides [58,59].

The iron oxide phases in the oxygen carriers lose a substantial amount of oxygen under a highly reducing environment. This led to the formation of iron oxide phases with low

oxidation numbers, such as wüstite (FeO) and elemental iron (Fe). Both the XRD results and observation under SEM/EDX suggest that the phase of elemental iron was formed on the surface of the most reduced iron-based oxygen carriers. From further thermodynamic analyses, it was hypothesized that the formation of elemental iron likely took place during reduction with the methane pulse instead of syngas. This was logical considering that the oxygen carrier has already been very reduced at this stage.

The oxidation reaction of any iron oxide phase is always exothermic; thus, generating heat and increasing the temperature inside the bed particles. The oxidation of elemental iron, wüstite, and magnetite to the fully oxidized phase, hematite, follows the reactions below. The standard heat of reaction per mole of released oxygen is also provided.

$$\frac{4}{3}Fe_{(s)} + O_{2(g)} \rightarrow \frac{2}{3}Fe_2O_{3(s)} \qquad \Delta H^o = -553.7\ kJ\ mol\ {O_2}^{-1} \qquad (4.1)$$

$$4Fe_3O_{4_{(s)}} + O_{2(g)} \rightarrow 6Fe_2O_{3(s)} \qquad \Delta H^o = -516.4\ kJ\ mol\ {O_2}^{-1} \qquad (4.2)$$

$$4FeO_{(s)} + O_{2(g)} \rightarrow 2Fe_2O_{3(s)} \qquad \Delta H^o = -579.6\ kJ\ mol\ {O_2}^{-1} \qquad (4.3)$$

The observed temperature increase inside the bed particle during oxidation was up to 15 °C higher than the set reaction temperature, yet the local temperature on the particle surface could have been higher due to the oxidation occurring at a specific active site. Should this local temperature exceed the melting points of the corresponding iron oxide phases, bed agglomeration could occur and cause bed defluidization. The bed sintering can even take place at a much lower temperature, known as Tamman temperature [60]. Table 4.3 below provides the melting temperature of relevant iron-based phases.

Table 4.3 The melting points of several iron-based phases.

Phases	Melting point, T_m (°C)
Fe_2O_3	1,565
Fe_3O_4	1,597
$FeTiO_3$	1,470
FeO	1,377
Fe	1,538

The sintering point of a pure metal solid solution was found to be about 0.67 – 0.75 T_m, but that of a mixed metal powder could be even lower [61]. Since the oxygen carriers used in this study are not pure, the sintering might have taken place between the oxygen carrier particles at a much lower temperature than the given melting points. This likely contributes to the fact that defluidization was observed under oxidation in this work.

Furthermore, the structure of oxygen carrier may change during the reduction, especially concerning the distribution of iron. The analysis was carried out by comparing what the elemental distribution within an oxygen carrier particle looked like

before and after defluidization. Figure 4.3 below illustrates the change in the elemental distribution detected with SEM/EDX.

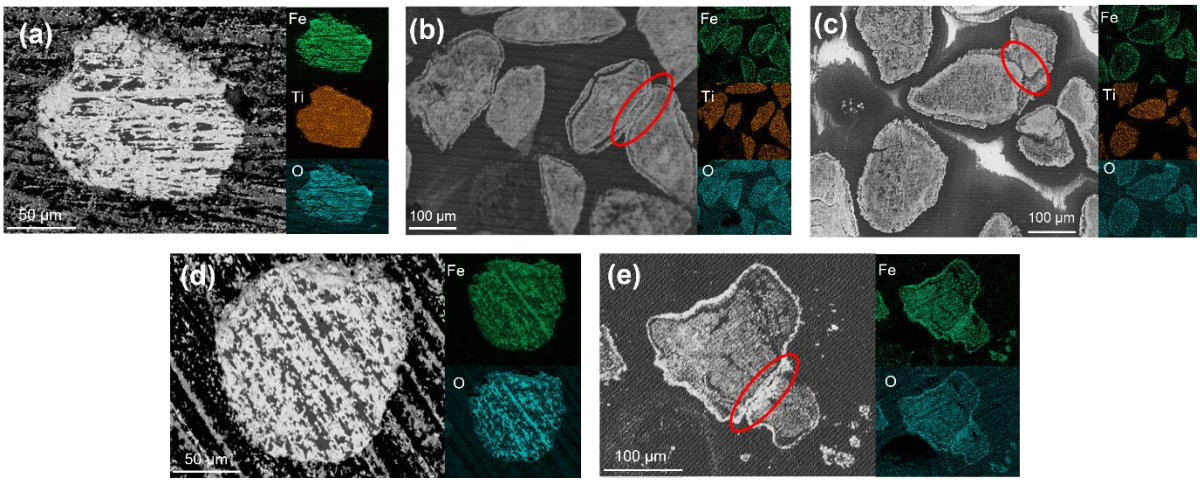

Figure 4.3 The elemental distribution of iron, titanium, and oxygen within (a) fresh ILFC, (b) defluidized ILFC, (c) defluidized ILAU, (d) fresh TOFC, and (e) defluidized TOFC. The red circles indicate interparticle joints.

In both ilmenite and Tierga ores, iron clearly migrated toward the outer surface of the oxygen carrier particles when defluidization occurred. This demonstrates that the structural changes taking place under a highly reducing environment. As explained above, the layers are likely iron that melted and formed interparticle joints, which then triggered agglomeration and, eventually, defluidization. On the other hand, oxygen also showed some denser clusters on the surface, which might indicate that the layers still probably comprise some iron oxides, most likely FeO. A previous study found the same pattern of iron migration under highly reducing conditions [59,62].

A high degree of reduction may not be relevant in a normal CLC or OCAC operation, yet such a situation may occur, at least locally, in a system where the partial oxidation of fuel is required, e.g., in CLG, CLR, or CLWS. In any process, agglomeration caused by high degrees of reduction may also occur in certain local zones of a reactor, for example close to the fuel inlet. This finding is useful for engineering design purposes, e.g., establishing applicable operational parameters, such as flow optimization, as well as a strategy to minimize the risk for agglomeration in certain zones.

4.1.2 Attrition resistance

Attrition resistance is a crucial parameter in material screening and an important parameter for material stability. The lower the attrition rate, the higher the expected lifetime of an oxygen carrier is. Here, the aim is to correlate the oxidation degree, which also includes high degrees of reduction, with the attrition rate.

In the investigations done in Paper V and VI, the basis experimental works are similar. Firstly, the oxygen carrier was exposed to ten activating redox cycles and eventually reduced to certain mass conversion degrees in a fluidized bed batch reactor. Table 4.4 shows the mass conversion degrees of the oxygen carriers after the eleventh cycle.

Table 4.4 Mass conversion degree of the oxygen carrier samples.

Oxygen carriers	Fully oxidized (FO)	Moderately reduced (MR)	Substantially reduced (SR)
Ilmenite ore	1.000	0.991	0.980
Synthetic ilmenite	1.000	0.990	0.979
Iron sand	1.000	0.992	0.983
LD slag	1.000	0.993	0.988
Mill scale	1.000	0.958	0.914

Among all the investigated samples, mill scale was able to undergo the furthest reduction without experiencing defluidization. This is because the material contains almost about 95 wt.% iron oxide (see Table 3.1) [63], implying a substantially higher oxygen transfer capacity, thereby allowing further reduction. Materials like ilmenite ore have been known for their defluidization tendency when exposed to a high reduction degree [38], thus the reduction extent was limited to avoid undesired defluidization in the fluidized bed. In the light of mass conversion degree changes, the crystalline phases on the oxygen carriers obtained from the XRD analysis using a molybdenum source are presented in Table 4.5.

Table 4.5 Crystalline phases on oxygen carriers' surface observed by XRD.

Oxygen carrier	Mass conversion degree	Crystalline phases
Ilmenite ore	1.000 (freshly calcined)	Fe_2TiO_5, Fe_2O_3, TiO_2
	1.000 (fully oxidized)	Fe_2TiO_5, Fe_2O_3, TiO_2
	0.991	Fe_2TiO_5, $FeTiO_3$, TiO_2
	0.980	Fe_2TiO_5, Fe_2O_3, Fe_3O_4, TiO_2
Synthetic ilmenite	1.000 (freshly calcined)	Fe_2TiO_5, Fe_2O_3, TiO_2
	1.000 (fully oxidized)	Fe_2TiO_5, Fe_2O_3, TiO_2
	0.990	Fe_2TiO_5, $FeTiO_3$, TiO_2
	0.979	Fe_2TiO_5, $FeTiO_3$, TiO_2
Iron sand	1.000 (freshly calcined)	Fe_2O_3, Fe_3O_4, SiO_2
	1.000 (fully oxidized)	Fe_2O_3, Fe_3O_4, SiO_2
	0.992	Fe_2O_3, Fe_3O_4, Fe_2SiO_4, SiO_2
	0.983	Fe_2O_3, Fe_3O_4, FeO, SiO_2
LD slag	1.000 (freshly calcined)	Fe_2O_3, Fe_3O_4, $Ca_2Fe_2O_5$, Ca_2SiO_4, CaO
	1.000 (fully oxidized)	Fe_2O_3, Fe_3O_4, $Ca_2Fe_2O_5$, Ca_2SiO_4, CaO
	0.993	Fe_3O_4, $Fe_{11}O_{12}$, $Ca_2Fe_2O_5$, Ca_2SiO_4, CaO
	0.988	Fe_3O_4, $Fe_{1-\delta}O_{12}$, $Ca_2Fe_2O_5$, Ca_2SiO_4, CaO
Mill scale	1.000 (freshly calcined)	Fe_2O_3
	1.000 (fully oxidized)	Fe_2O_3
	0.958	Fe_3O_4, FeO
	0.914	Fe_3O_4, FeO, $Fe_{1-\delta}O$, Fe

During the investigations using the customized jet cup device, each material showed a different attrition rate tendency [48]. Figure 4.4 below illustrates the different attrition rate tendencies (see Eq. 3.7 for calculation) observed with ilmenite ore. Here, A_{tot} and $A_{30\text{-}60}$ refer to the total attrition rate observed during the whole 60-minute investigation and the attrition rate in the last 30 minutes in the observation, respectively. Freshly calcined ilmenite ore tends to experience a linear total attrition [64], while the fully oxidized one follows a non-linear trend.

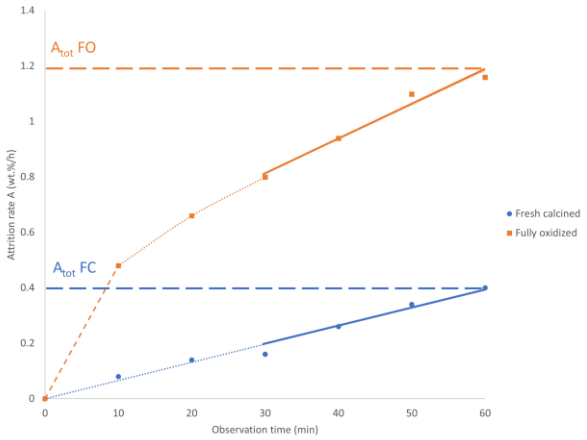

Figure 4.4 Different attrition rate tendencies observed on the freshly calcined (FC) and fully oxidized (FO) ilmenite ore, which show linear and non-linear total attrition trends, respectively. The solid and dashed lines refer to the attrition rate $A_{30\text{-}60}$ and A_{tot}, respectively.

The total attrition rate of most oxygen carrier samples follows a non-linear trend. Still, the attrition rate in the last 30 minutes of all samples during the observations tends to show a rather linear trend [48] (see the solid lines in Fig. 4.4). Therefore, this attrition rate, symbolized as $A_{30\text{-}60}$, can be taken as the basis of linear comparison.

Figure 4.5 shows the attrition rate $A_{30\text{-}60}$, presented in bar columns, measured for different oxygen carrier materials at different mass conversion degrees, refer to left y-axis. Additionally, the attrition rate ratio between $A_{30\text{-}60}$ and A_{tot} is also presented as line in the same graph, refer to the right y-axis. An attrition rate of 1 indicates a perfectly linear attrition [48]. Sand is shown as a reference. With respect to attrition rate ratio, most oxygen carriers, except synthetic ilmenite, show an either similar or lower attrition rate ratio than that of sand. Only LD slag shows a declining attrition rate ratio, while the other materials tend to show a rather stable attrition rate ratio.

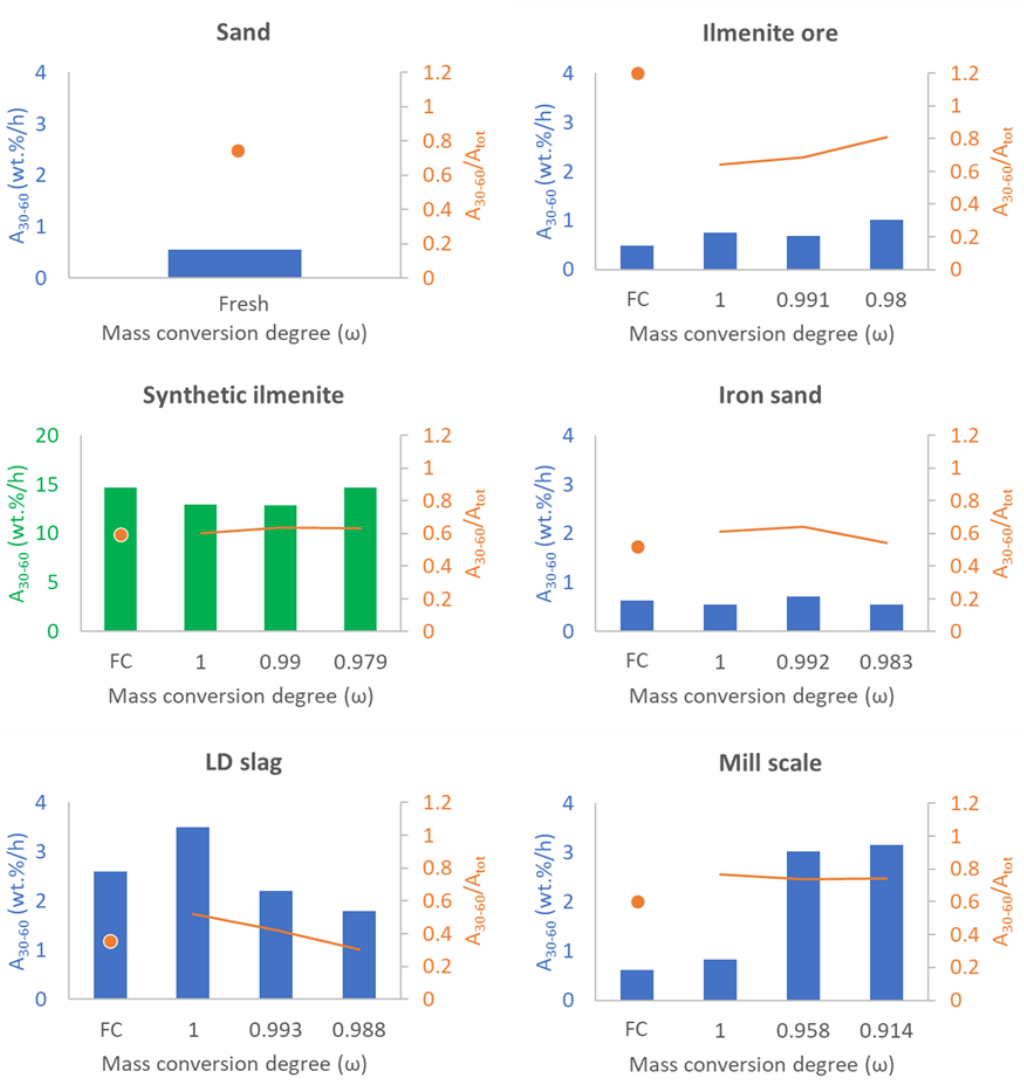

Figure 4.5 The attrition rate $A_{30\text{-}60}$ (presented in bar columns) and the attrition rate ratio $A_{30\text{-}60}/A_{tot}$ (presented as lines) for different oxygen carriers at different mass conversion degrees. FC denotes the freshly calcined state of each material. Note that the synthetic ilmenite has a different Y-axis scale for $A_{30\text{-}60}$.

The attrition rate tendency changes between different materials. Sand as the reference material, which is a common bed material in circulating fluidized bed units, has an attrition rate and an attrition rate ratio of around 0.5 wt.%/h and 0.75, respectively. Ilmenite ore saw a slightly increasing attrition rate with an average value slightly higher than sand. This makes ilmenite ore one of the most robust materials with quite a stable attrition rate in this study. The material has been reported to have a low attrition rate in a chemical looping combustion units [65], so this was expected. On the other hand, synthetic ilmenite has shown the highest attrition rates among the evaluated oxygen carriers at all mass conversion degrees. This is even though the material has undergone a similar crystalline phase transformation with ilmenite ore.

To analyze this further, it is worth looking at the composition of fines collected from the jet cup rig, examined under SEM/EDX, and the semi-quantitative (S-Q) analysis of the bulk oxygen carriers' surface before examination in the jet cup rig, which can be found in Paper V. Both analyses clearly show iron enrichment on the surface of substantially reduced ilmenite ore compared to its fully oxidized counterpart, which is not observed in synthetic ilmenite. The major reason for this phenomenon is likely due to the synthesis process itself, which led to loosely sintered Fe_2O_3 and TiO_2 particles. Contrary to the ilmenite ore, which had undergone harsher geological processes over millennia, synthetic ilmenite has only been exposed to a much quicker heat treatment. Furthermore, Staničić et al. [66] has reported that synthetic ilmenite tends to be more porous than ilmenite ore. A higher porosity has been reported to be one of the factors that cause a decreased attrition resistance [64,67].

The SEM observations in Fig. 4.6 show that freshly calcined ilmenite ore has a more uniform sintered surface compared to freshly calcined synthetic ilmenite. On the other hand, Fig. 4.7 visualizes that the collected fines from fully oxidized ilmenite ore are significantly coarser and do have sharper edges compared to that from fully oxidized synthetic ilmenite; indicating that the former tends to be able to withstand attrition better than the latter.

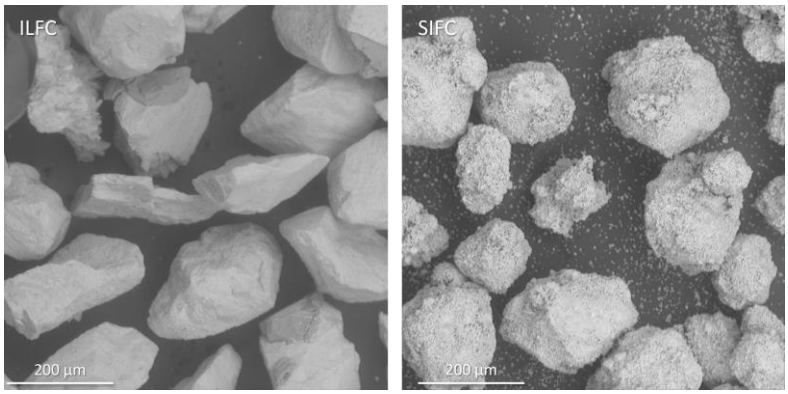

Figure 4.6 SEM images of freshly calcined ilmenite ore (ILFC) and synthetic ilmenite (SIFC).

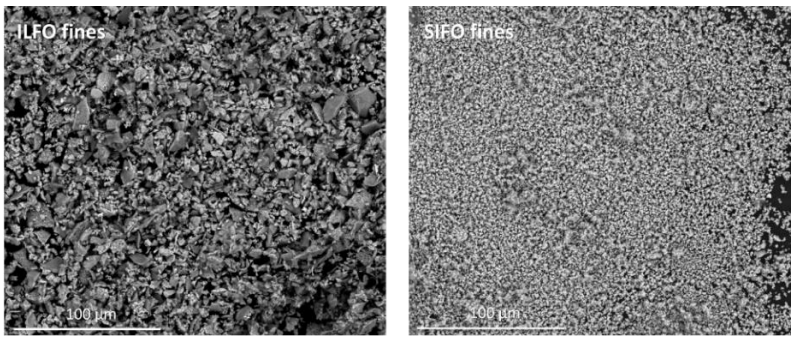

Figure 4.7 SEM images of collected fines from attrition examinations of fully oxidized ilmenite ore (ILFO) and synthetic ilmenite (SIFO) in the customized jet cup rig.

Among the investigated waste materials, namely iron sand, mill scales, and LD-slag, iron sand has shown quite a stable attrition resistance, and its attrition rates are high; on par with those of ilmenite. The reported BET surface area of freshly calcined iron sand indicate a rather low porosity [32], which may contributes to its mechanical stability as is the case with ilmenite ore. It was also observed that freshly calcined iron sand is quite difficult to break into smaller pieces.

LD slag generally shows higher attrition rates compared to ilmenite ore. Some manganese ores with a significant CaO content have shown a similar attrition rate to LD slag in this study [68]. The fact that LD slag has multiple phases on its surface (see Table 4.5) may have led to a rather uneven phase distribution and, therefore, uneven strength throughout the particle. This likely causes a lower attrition resistance. Interestingly, the attrition rate of LD slag tends to decrease as a function of decreasing mass conversion degree, which is counter intuitive. Hildor et al. [69] reported a decrease on the BET surface area of LD slag after activation, which suggests that the material becomes less porous during redox cycles. These likely have an implication to the increasing trend of its attrition resistance.

Mill scale has previously been reported to have a lower attrition resistance compared to ilmenite ore [70], so it is reasonable that the material has significantly higher attrition rates at lower mass conversion degrees. The attrition resistance and crushing strength of mill scale tends to decrease as the material gets reduced further. Table 4.5 demonstrates that the freshly calcined mill scale has an almost completely homogeneous hematite, but its substantially reduced counterpart comprises largely magnetite and minor amounts of wüstite and elemental iron. The formation of these phases reportedly leads to more cracks and pores visible on the oxygen carrier's surface [71]. This may contribute to a decreasing attrition resistance of mill scale at lower mass conversion degrees.

No strong correlation can be deduced between the phase transformation and attrition rate, but one can attempt to see if there is any correlation between the main metal bases and the attrition rate. Table 4.6 summarizes the main metal bases, the ratio of average attrition rates of the activated samples (taken from three different mass conversion degrees – the freshly calcined sample is excluded) to that of sand (see Fig. 4.4), and the attrition rate trend of the evaluated oxygen carriers.

Table 4.6 Main metal bases, ratio of average attrition rate to that of sand, and attrition rate trend of examined oxygen carriers.

Oxygen carrier	Main metal bases	Ratio of average attrition rate to that of sand	Attrition rate trend over decreasing mass conversion degree
Ilmenite ore	Fe, Ti	1.4	Generally stable
Synthetic ilmenite	Fe, Ti	24.4	Generally stable
Iron sand	Fe, Si	1.1	Generally stable
LD slag	Fe, Ca	4.5	Decreasing
Mill scale	Fe	4.2	Increasing

From Table 4.6, it seems that both Fe-Ti and Fe-Si combinations contribute to a rather stable attrition rate over different mass conversion degrees. Furthermore, materials with these combinations show a comparable attrition rate to sand, except for synthetic ilmenite – this has been explained above. On the other hand, Fe alone tends to see a decrease in attrition resistance with further reduction, while an Fe-Ca system seems to contribute to an improved attrition resistance at lower mass conversion degrees. Our hypothesis is that this can be related to the physicochemical structure of the materials and how it changes with reduction [72]. This may include multiple factors such as porosity [73,74], sintering quality, and formation of iron layers [75]. Still, this hypothesis may need to be investigated further in the future.

This finding should be considered in the screening of materials. For instance, even if an oxygen carrying material shows an acceptable reactivity, a low mechanical stability implies an unfavorable lifetime of the oxygen carriers. From this perspective, it would probably be wise to reject such a material due to practical and economic reasons.

4.1.3 Particle size and shape analysis

Particle size and shape analysis can in some way demonstrate the suitability and stability of an oxygen-carrying material. Any bed particles should ideally have a relatively high sphericity to allow a more homogeneous mixing in the fluidized bed [76]. Specifically, an oxygen carrier should not experience significant changes in size and shape during exposure to redox cycles in fluidized bed. It has been reported that particle size and shape of bed particles may influence hydrodynamics in fluidized bed [77,78] as well as interactions with ash compounds in biomass [79]. Both can influence fluidization performance and fuel conversion. Therefore, performing particle size and shape analysis on oxygen carriers is highly relevant to the field.

With respect to the investigations done in Paper VI, the particle width, sphericity, and aspect ratio of various iron oxygen carrier samples were analyzed in the particle size analyzer Camsizer XT and visualized in Fig. 4.8. The list of materials includes freshly calcined and activated oxygen carriers, see Tables 4.4, as well as sand as reference. The detected crystalline phases at different oxidation degrees can be found in Table 4.5. It is important to note that the original sieving size range for all materials is 125 – 180 μm. This is despite the fact that some samples, e.g., all the LD slag samples, deviate significantly from this size range. The deviation of LD slag samples was likely due to the intrinsic traits of the material itself which can break easily into fines and form satellite particles due to its heterogeneous composition [5]. The plots are restricted to values between 1 and 99% of the cumulative distribution range. The cumulative distribution percentage obtained from the analysis is expressed in volume percentage, which is deemed suitable to visualize a representative particle size distribution according to ISO 9276-1:1998 [80].

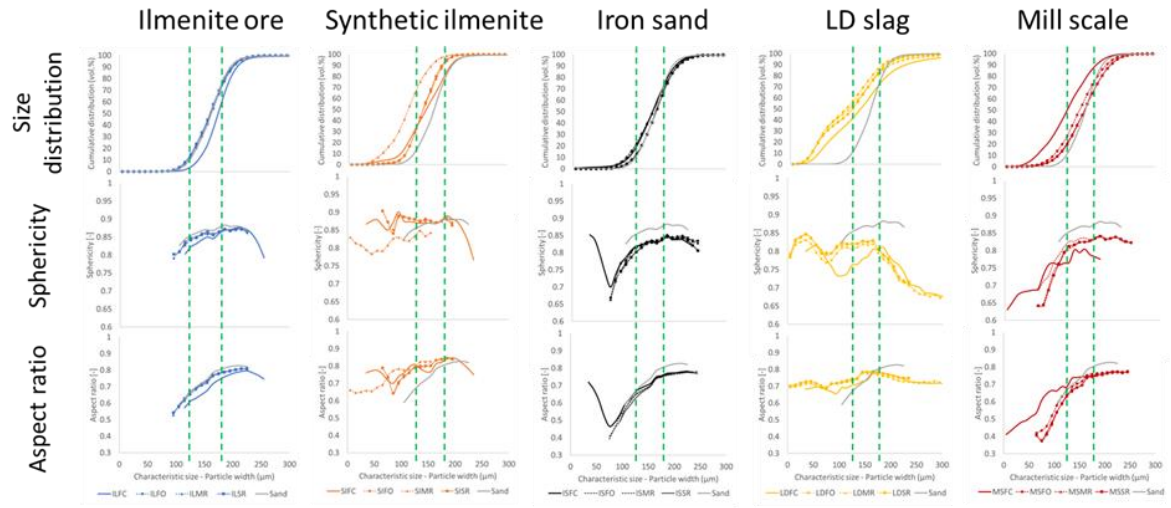

Figure 4.8 Measured sphericity and aspect ratio of the investigated oxygen carrier samples, both freshly calcined and activated (with different oxidation degrees), and sand plotted against characteristic size. The green dashed lines indicate the original sieving size range (125 – 180 μm).

In terms of particle size of the activated materials (fully oxidized, moderately reduced, and substantially reduced – see Table 4.4), the results demonstrate that oxidation degree only influences the particle size distribution of oxygen carrier materials to a minor extent. Nevertheless, the contrast is prominent when comparing the freshly calcined to the activated materials, e.g., the fully oxidized one. While ilmenite ore and iron sand are the least affected, which is not surprising as these materials have shown a robust attrition resistance, there is still a small difference on the particle size distribution of their freshly calcined and activated forms. A clear difference is presented for the freshly calcined forms of synthetic ilmenite and LD slag, which are coarser than their respective activated samples, while mill scale shows the opposite phenomenon.

The average sphericity and aspect ratio of both freshly calcined and activated oxygen carriers are presented in Paper VI. The results demonstrate two main findings:
i) There is no significant difference in average sphericity and aspect ratio between freshly calcined and activated oxygen carriers.
ii) The average sphericity and aspect ratio of all oxygen carriers remain relatively stable over different oxidation degrees.
In general, a sphericity of 0.78 – 0.86 can be assumed for oxygen carrier materials for practical applications. This aligns with a previous study by Schwebel et al. [52] which assumed the sphericity of an ilmenite ore at the same size range to be 0.79. The aspect ratios of oxygen carriers generally lie between 0.65 and 0.73. According to Blott and Pye [81], the investigated oxygen carrier materials generally have a high sphericity and can be categorized as slightly elongated particles. These demonstrate that particle size

and shape of the investigated oxygen carriers are highly stable as they tend to remain unchanged in this study. Therefore, it is not expected that the particle size and shape of oxygen carriers alone will affect the fluidization performance and fuel conversion (with respect to the mixing quality) in a chemical looping unit significantly. However, these results should be considered complimentary to attrition rate for the purpose of screening oxygen-carrying materials and determining material stability.

4.2 Reactivity and fuel conversion

One of the most important properties of oxygen carriers which determines their suitability for utilization in a chemical looping or even OCAC unit is their reactivity in converting fuel. Unsurprisingly, the study of reactivity of oxygen carriers has been the main focuses of a considerable amount of publications in the past decades [32,52,82–98]. Nonetheless, this does not mean that further studies are no longer necessary. High degrees of reduction may affect both the reactivity of oxygen carriers and fuel conversion. The reactivity of oxygen carriers is expected to decrease at high degrees of reduction. In order to establish a thorough analysis in this regard, the apparent kinetics, and how if varies with reduction degree, for three iron-based oxygen carriers during conversions of common gaseous fuels: CO, H_2, and CH_4 were studied and are presented here. On the other hand, the conversion rate of solid char, such as pine forest residue in this study, may also be affected by high degrees of reduction. This is because the production of rate-inhibiting gaseous agents, such as CO and H_2, are generally enhanced at lower degrees of oxidation. How this affected the gasification rate of pine forest residue is in this work compared when using ilmenite and iron sand as oxygen carriers. This is relevant for design purposes with respect to biomass conversion in chemical looping processes, especially chemical looping gasification (CLG).

4.2.1 Apparent kinetics of oxygen carriers

Since high degrees of reduction is involved in this work, it is expected that the reactions involved in this work is not only reduction of hematite to magnetite, but also reduction of magnetite to wüstite [32,38]. This is especially relevant to processes where oxygen carriers may experience such situations, such as chemical looping gasification, reforming, and water splitting [99]. Table 4.7 summarizes the investigated mass conversion degree, possible reactions taking place during the reductions, and the maximum gas yield of fuel *i* ($\gamma_{i,max}$) allowed by the thermodynamics at 900 °C. The calculations were performed using FactSage 8.2 utilizing the pure substance database [100].

Table 4.7 Possible reduction reactions taking place during the reductions and their respective maximum thermodynamic gas yield of gaseous fuel *i* ($\gamma_{i,max}$) at 900 °C.

Oxygen carrier	Fuel	Investigated mass conversion degree	Possible reactions	$\gamma_{i,max}$* at 900 °C
Ilmenite	CO	0.999 – 0.951	$Fe_2TiO_5 + TiO_2 + CO \rightarrow 2FeTiO_3 + CO_2$ $3Fe_2O_3 + CO \rightarrow 2Fe_3O_4 + CO_2$ $Fe_3O_4 + CO \rightarrow 3FeO + CO_2$	0.999 0.999 0.693
	H_2	0.997 – 0.954	$Fe_2TiO_5 + TiO_2 + H_2 \rightarrow 2FeTiO_3 + H_2O$ $3Fe_2O_3 + H_2 \rightarrow 2Fe_3O_4 + H_2O$ $Fe_3O_4 + H_2 \rightarrow 3FeO + H_2O$	0.999 0.999 0.739
	CH_4	0.999 – 0.950	$4Fe_2TiO_5 + 4TiO_2 + CH_4 \rightarrow 8FeTiO_3 + CO_2 + 2H_2O$ $12Fe_2O_3 + CH_4 \rightarrow 8Fe_3O_4 + CO_2 + 2H_2O$ $4Fe_3O_4 + CH_4 \rightarrow 12FeO + CO_2 + 2H_2O$	0.999 0.999 0.693
Iron sand	CO	0.999 – 0.977	$Fe_2O_3 + SiO_2 + CO \rightarrow Fe_2SiO_4 + CO_2$ $3Fe_2O_3 + CO \rightarrow 2Fe_3O_4 + CO_2$ $Fe_3O_4 + CO \rightarrow 3FeO + CO_2$	0.998 0.999 0.693
	H_2	0.995 – 0.971	$Fe_2O_3 + SiO_2 + H_2 \rightarrow Fe_2SiO_4 + H_2O$ $3Fe_2O_3 + H_2 \rightarrow 2Fe_3O_4 + H_2O$ $Fe_3O_4 + H_2 \rightarrow 3FeO + H_2O$	0.998 0.999 0.739
	CH_4	0.999 – 0.983	$4Fe_2O_3 + 4SiO_2 + CH_4 \rightarrow 4Fe_2SiO_4 + CO_2 + 2H_2O$ $12Fe_2O_3 + CH_4 \rightarrow 8Fe_3O_4 + CO_2 + 2H_2O$ $4Fe_3O_4 + CH_4 \rightarrow 12FeO + CO_2 + 2H_2O$	0.998 0.999 0.693
LD slag	CO	0.998 – 0.958	$3Fe_2O_3 + CO \rightarrow 2Fe_3O_4 + CO_2$ $Fe_3O_4 + CO \rightarrow 3FeO + CO_2$	0.999 0.693
	H_2	0.995 – 0.974	$3Fe_2O_3 + H_2 \rightarrow 2Fe_3O_4 + H_2O$ $Fe_3O_4 + H_2 \rightarrow 3FeO + H_2O$	0.999 0.739
	CH_4	0.999 – 0.977	$12Fe_2O_3 + CH_4 \rightarrow 8Fe_3O_4 + CO_2 + 2H_2O$ $4Fe_3O_4 + CH_4 \rightarrow 12FeO + CO_2 + 2H_2O$	0.999 0.693

* $\gamma_{CO,max} = \frac{p_{CO2}}{p_{CO_2}+p_{CO}}$ $\gamma_{CH_4,max} = \frac{p_{CO2}}{p_{CO_2}+p_{CO}+p_{CH_4}}$ $\gamma_{H_2,max} = \frac{p_{H2O}}{p_{H_2O}+p_{H_2}}$

By comparing the maximum yield observed during the experiment to the theoretical maximum yield allowed by thermodynamics at 900 °C for each individual reaction presented in Table 4.7, Fig. 4.9 demonstrates that the reactions investigated in this thesis were not thermodynamically limited. With respect to the conversion of Fe_2O_3 to Fe_3O_4 (as well as Fe_2TiO_5 + TiO_2/$FeTiO_3$ and Fe_2O_3 + SiO_4/Fe_2SiO_4), the maximum thermodynamic limit is always above 99.8%. Such a limit was not reached during experimental conditions for CO and CH_4. For H_2, on the other hand, an almost complete conversion was achieved at high mass conversion degrees (ω > 0.995) and, thus, the corresponding experimental points are close to thermodynamic equilibrium. Due to this, the reactivity with H_2 for iron sand and LD slag was only examined at mass conversion degrees lower than 0.995.

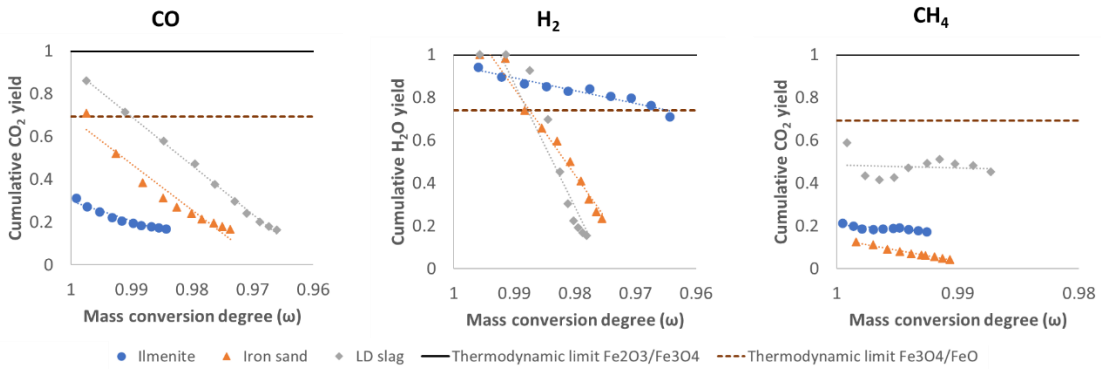

Figure 4.9 Observed maximum gas yields for ilmenite (blue), iron sand (orange) and LD slag (grey) at 900°C for three fuels presented in panel a) CO, b) H_2 and c) CH_4. Every point represents one pulse of fuel. The theoretical gas conversion limitations of Fe_2O_3/Fe_3O_4 and Fe_3O_4/FeO are shown as solid and dashed lines, respectively.

Another thermodynamic limit that might need to be considered is Fe_3O_4/FeO. As shown in Fig. 4.9, some of the experimental values, especially in case of reactions with H_2, are found to be above this limit. However, it should be noted that the reactions listed in Table 4.7 may not likely happen at the same time. The most logical and likely scenario is that conversion of Fe_2O_3 to Fe_3O_4 takes place at higher mass conversion degree, followed by reduction of Fe_3O_4 to FeO at lower mass conversion degrees [101]. Therefore, this theoretical limit is probably less relevant for this work, especially at higher mass conversion degrees. Note that the oxygen carriers were always fully oxidized prior to the apparent kinetic investigation. Thus, the more applicable limit for this work would be Fe_2O_3/Fe_3O_4.

The kinetic parameters were determined according to the procedure explained in sub-section 3.6.1. To reiterate, the best model chosen in this study is the one that fulfills these conditions:
a) Showing the highest linearity in step (i) based on the Pearson correlation coefficient, see Eq. 3.14 [95], over different temperatures, and
b) Showing a physically reasonable trend in the plot of reactivity, symbolized as r_i, (Eq. 3.12) vs mass conversion degree, symbolized as ω.
c) Predicting the closest reactivity to the experimental data.
The chosen model was the basis to calculate the rate constant $k(T)$ in step (ii) as well as the activation energy E_a and pre-exponential factor k_0 in step (iii).

With respect to criteria (i), models with the highest Pearson coefficient correlation seem to vary depending on the type of oxygen carriers and gaseous fuels. This can be seen in Paper IV. However, it turns out that only a high R^2 value is not sufficient. Other criteria must also be fulfilled in order to establish a reliable model fitting. There are two types of issues observed with models with the highest R^2: physically unreasonable reactivity

trend (e.g., the reactivity increases at lower mass conversion degrees), and significantly overestimated reactivity.

Further analyses prove that the changing grain size (CGS) model seems to be the most applicable model as this model can predict reactivity values that are the closest to the experimental ones in most cases. The solid-state kinetic formulae *f(ω)* and *g(ω)*, which correspond to the derivative and integrated forms, respectively, of the CGS model are shown below. Note that these were converted from the respective *f(α)* and *g(α)* functions provided in Paper IV.

$$f(\omega) = \frac{3R_O\bar{b}\left(1-\frac{\omega-1}{R_O}\right)^{2/3}}{\rho_m r_{OC}} \tag{4.4}$$

$$g(\omega) = \frac{\rho_m r_{OC}}{\bar{b}}\left[1-\left(\frac{\omega-1}{R_O}\right)^{1/3}\right] \tag{4.5}$$

Even though the basic formula of CGS is similar to the volume-based geometrical contraction model (R3) [52,82,89], see Paper IV, this model also considers parameters such as grain size, stoichiometric coefficient, and gas molar density. None of the other models take these factors into account, so they tend to overestimate the reactivity values despite the high correlation coefficient (R^2). Table 4.8 shows the coefficient correlation R^2 as well as the obtained kinetic parameter for each oxygen carrier – gaseous fuel pair when using CGS model.

Table 4.8 Kinetic parameters for each oxygen carrier – gaseous fuel pair obtained using CGS model.

Oxygen carrier	Gaseous fuel	Investigated temperatures (°C)	R^2	k_0 (s^{-1})	E_a (kJ/mol)
Ilmenite	CO	850, 900, 950, 975	0.8809	0.003	91.6
	H_2	850, 875, 900, 950	0.9895	$1*10^5$	251
	CH_4	850, 875, 900, 950	0.9507	137	211
Iron sand	CO	850, 875, 900, 950	0.9387	$2.2*10^{-5}$	51.5
	H_2	850, 875, 900, 925, 950	0.9662	6.6	161
	CH_4	850, 875, 900, 950	0.9395	$2.3*10^{-5}$	72.4
LD slag	CO	850, 875, 900, 950	0.8719	$4*10^{-4}$	74.8
	H_2	850, 875, 900, 950	0.9479	$8*10^{-4}$	55.5
	CH_4	850, 875, 900, 950	0.9468	0.004	122

The fittings of reactions with CO in Table 4.8 show a much lower Pearson correlation coefficient (R^2) compared to those with H_2 and CH_4. This is because the plots of $g(\alpha)$ versus time for reactions with CO do not show a continuous linear line, but rather different stages of correlation at different time periods. These likely correspond to different reaction mechanisms for different iron oxide phases, which have been discussed in Paper IV. It should be noted that the main purpose of this part of the thesis is to establish applicable apparent kinetics for reactions between the investigated oxygen carriers and gaseous fuels, and this has been delivered here. The results successfully demonstrate that CGS model is applicable for apparent kinetic analysis of reactions between iron oxygen carriers and CO, H_2, and CH_4 even at lower oxidation degrees (3 – 5 wt.% reduction). Therefore, this model can be used for various engineering design purposes, such as designing a fuel reactor. Note that the gaseous fuels used in this work are also commonly present in volatile contents in biomass, so these results are relevant also in the case of biomass conversion.

4.2.2 Solid fuel conversion

In this work, pine forest residue char was used as solid fuel. This type of biomass is commonly used in both combustion and gasification [102,103] The reactivity of pine forest residue char during a steam char conversion in the fluidized bed batch reactor was investigated using two iron-based oxygen carriers: ilmenite ore (Paper II) and iron sand (Paper III). Ilmenite ore can be considered as the benchmark chemical looping oxygen carrier and many studies have been performed on this material to investigate its performance and suitability as an oxygen carrier; the material has also been used as an oxygen carrier in commercial scale OCAC units [13]. Iron sand, on the other hand, is a new oxygen carrier candidate that is less explored and that has just recently been studied

in a fluidized bed system in Paper III. However, a recent campaign in a circular fluidized bed unit at Chalmers University of Technology indicates that iron sand performed quite well as bed material in this semi-commercial unit. Comparing the reactivity of a biomass-based char toward these oxygen carriers is, thus, highly interesting, especially at higher reduction degrees. In CLG, for instance, one can expect that the oxygen carrier will only be partially oxidized in the air reactor. This is done to maintain the partial oxidation of fuel during the gasification in the fuel reactor. Figure 4.10 compares both the hydrogen partial pressure and char conversion rate toward ilmenite ore and iron sand in the fluidized bed batch reactor, as well as the validation of three Langmuir – Hinshelwood mechanism models, at various mass conversion degrees.

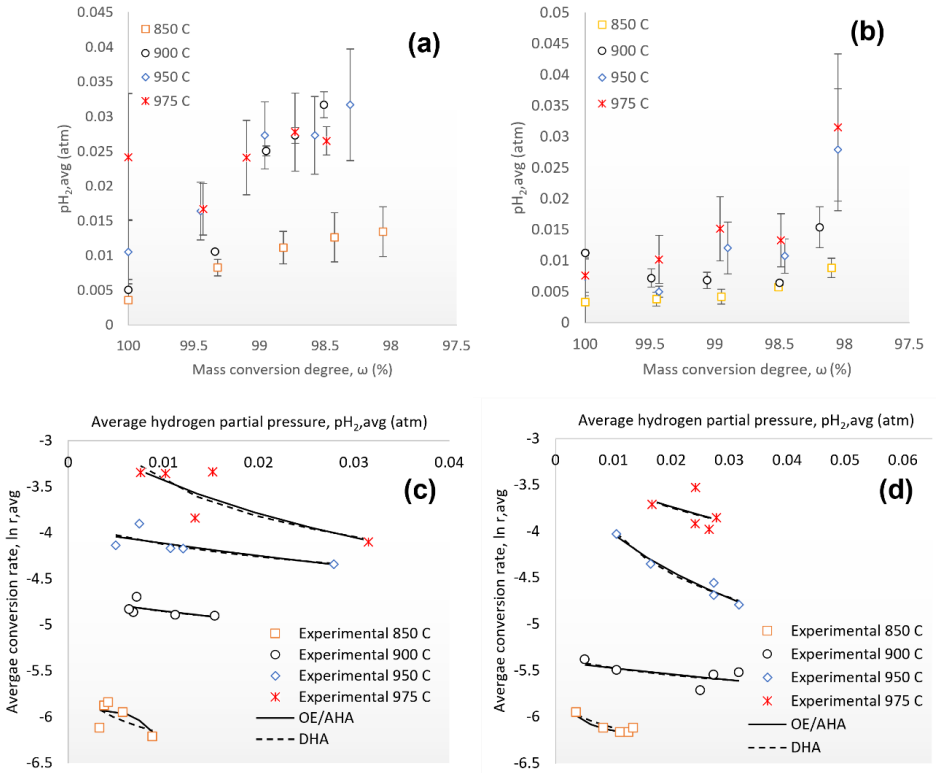

Figure 4.10 The hydrogen partial pressure during pine forest residue char conversion as a function of mass conversion degree, which was set by diluted CO injection, using (a) ilmenite ore and (b) iron sand as oxygen carriers. The conversion rate of the char using (c) ilmenite ore and (d) iron sand is plotted as a function of the hydrogen partial pressure to validate the Langmuir – Hinshelwood mechanism models.

In general, hydrogen partial pressure increases at lower mass conversions degrees. The hydrogen generated from the char conversion using ilmenite ore does not differ significantly from that of iron sand. The hydrogen partial pressure caused by changes in the mass conversion degree alone was quite low; this could be due to the high dilution by steam and nitrogen. Still, the study was able to confirm that the mass conversion degree did affect the hydrogen partial pressure, especially at higher temperatures of 950

and 975 °C; the lower the mass conversion degree was, the higher hydrogen partial pressure became. This could be due to the equilibrium shift in the water-gas shift reaction [104] shown in Eq. 4.6 below, which was caused by the exhausting available oxygen in the oxygen carrier.

$$CO + H_2O \rightleftharpoons CO_2 + H_2 \quad (4.6)$$

Another possible explanation is that the reactivity of oxygen carriers was decreased at higher reduction degrees, as reflected by the declining char conversion rate. Thus, the char conversion rate did become lower at higher hydrogen partial pressures. This can clearly be seen on the conversion of pine forest char using ilmenite ore and iron sand at 975 °C and ≥ 950 °C, respectively. This indicates that a higher hydrogen partial pressure led to a slower char conversion rate, which is known as the hydrogen inhibition effect [56]. Since the hydrogen partial pressure was confirmed as a function of mass conversion degree, it means the mass conversion degree had an indirect effect on the char conversion rate; the lower the mass conversion degree was, the higher the hydrogen partial pressure and the lower the char conversion rate.

The mechanism of hydrogen inhibition can be predicted by validating three Langmuir – Hinshelwood mechanism models, see Paper II, against the experimental data. This can be seen in Figure 4.10c and 4.10d. The obtained model parameters are provided in Table 4.9 below; note that the oxygen exchange (OE) and associative hydrogen adsorption (AHA) share the same rate formula.

Table 4.9 The obtained Langmuir – Hinshelwood model parameters for conversion of pine forest residue using ilmenite ore and iron sand.

Model	Rate equation and units	Oxygen carrier material	Parameters			
			850 °C	900 °C	950 °C	975 °C
OE/AHA	$r_c = \frac{1}{a + bpH_2}$ a in s, b in s.atm^{-1}	Ilmenite ore	a = 313.6 b = 18,296	a = 111.4 b = 1,621	a = 52.6 b = 876	a = 17.8 b = 1,325
		Iron sand	a = 369 b = 8,215	a = 222 b = 1,630	a = 28 b = 2,813	a = 26 b = 794
DHA	$r_c = \frac{1}{a + b\sqrt{pH_2}}$ a in s, b in s.atm$^{-0.5}$	Ilmenite ore	a = 224.5 b = 2,597	a = 95.2 b = 329.6	a = 41 b = 211	a = - 4.6 b = 356
		Iron sand	a = 304 b = 1,497	a = 195 b = 440	a = -25 b = 788	a = 10 b = 229

The validation shows that both OE/AHA and DHA models are close to each other, making it difficult to pinpoint which models are relevant. Based on the validation of the models in the conversion using ilmenite ore at 850 °C, it seems that OE/AHA fit the experimental data better than DHA; however, this cannot be used as a conclusion for all available data in both experiments using ilmenite ore and iron sand. One can reflect on a previous study by Lussier et al. [105], which used an annealed char in a temperature programmed desorption (TPD). The study suggested that all adsorbable hydrogen had already been consumed at 727 °C, eliminating the possibility for AHA and DHA at higher temperatures. Despite the different char used in this thesis, the finding is considered relevant given the fact that all the temperatures used in this study were higher than 727 °C. Therefore, the oxygen exchange mechanism was likely the relevant explanation of the hydrogen inhibition effect in this thesis for both materials.

Given the discussion, it seems that there is no significant difference between the reactivity of pine forest residue char toward ilmenite ore and toward iron sand. The use of ilmenite ore in CLG has been recommended in Paper II based on the reactivity results and physical performance observation, e.g., no defluidization was observed during the experiments despite the high reduction degree. Hence, iron sand with similar reactivity and fluidization performance will likely show a good performance in CLG as well. Furthermore, using ilmenite and iron sand should result in a similar char conversion rate and, therefore, fuel residence time. From a design perspective, this is desired as the fuel reactor design should not necessarily be altered when switching oxygen carrier from ilmenite to iron sand and vice versa. Still, the reactivity and physical performance of these oxygen carriers need to be considered with respect to material selection.

5. Conclusions

5.1 Summary

This thesis aims to present the behavior of iron-based oxygen carriers in deep reduction states, which is considered relevant to processes which require limited oxygen transfer or demand, such as chemical looping gasification or reforming. Assessing physical properties and performance of iron-based oxygen carriers are equally important to evaluating reactivity as well as fuel conversion. Both aspects are complementary to each other and should be considered thoroughly for various applicable purposes, such as material selection and engineering design.

Based on the work and discussion that have been undertaken during this doctoral study period, these takeaways can be concluded:

i) Defluidization of iron-based oxygen carriers can take place under highly reducing conditions, which is triggered by two factors: outward migration of iron during reduction process and the formation of iron oxide phases with a low oxidation number, such as wüstite (FeO) and/or elemental iron (Fe). Both factors contribute to the formation of melts which can create agglomerates and, thereby, lead to bed defluidization.

ii) The oxidation state of an oxygen carrier may affect its attrition rate to a certain extent, which can be due to the porosity change caused indirectly by crystalline phase transformation. While ilmenite ore and iron sand have shown a robust attrition resistance independent of mass conversion degree, LD slag and mill scale show an increasing and a decreasing attrition resistance as a function of decreasing mass conversion degree.

iii) Both exposure to redox cycles and mass conversion degree of an oxygen carrier generally shows an insignificant influence on its sphericity and aspect ratio, demonstrating the stability of oxygen carriers' size and shape. The investigated oxygen carrier materials generally have a high sphericity and are only slightly elongated.

iv) The apparent reactivity study of three iron oxygen carriers using model fitting methods show that the changing grain size (CGS) model is the most applicable solid-state models to predict the reactivity of the oxygen carriers in conversions of CO, H_2, and CH_4. This also applies at lower oxidation degrees (3 – 5 wt.% reduction).

v) There is no significant difference between using ilmenite ore and iron sand as oxygen carriers in terms of gasification rate of pine forest residue char in a fluidized bed batch reactor. This is despite the H_2 rate inhibition effect.

5.2 Future outlook

Considerable research effort has been done in this thesis to evaluate behavior of oxygen carriers at high degrees of reduction. This has yielded a deeper understanding of how oxygen carriers would likely behave in a chemical looping unit, especially chemical looping gasification, reforming, and water splitting. These processes aim to obtain valuable products, such as syngas and hydrogen, with the possibility for carbon capture. Thus, further studies in this field can contribute to the establishment of environmentally sound energy production technologies. It is expected that more applicable research effort will be conducted as these technologies emerge and eventually be commercialized.

Future relevant research work can focus on at least two objectives:

i) Characterization of materials

There will surely be other interesting materials, even the non-iron ones, to investigate as oxygen carriers in the future. Waste materials can be an attractive option as oxygen carriers if they show reasonable reactivity and good stability. This thesis has given an insight into which examination and criteria can be used for material screening. Still, there are other parameters to figure out that can be crucial to evaluate in the future. These may specifically include evaluating the effect of number of cycles, which involves high degrees of reduction, on attrition rate as well as particle size and shape. Furthermore, with respect to the use of biomass as fuel, interactions with alkali or ash compounds at high degrees of reduction in a fluidized bed are also interesting to investigate.

ii) Process optimization

In this thesis, the reactivity of oxygen carriers at high degrees of reduction and gasification rate of biomass char using different iron-based oxygen carriers have been investigated. Future research work can focus on the optimization of reactor design with respect to different relevant processes based on the presented work. Furthermore, further kinetic study can also be performed as research on chemical looping processes continues. For instance, chemical looping water splitting (CLWS) should comprise three, instead of two, reactors. The third reactor is called steam reactor, where oxygen carrier is oxidized with steam to produce hydrogen [106]. In this regard, it will be worth evaluating the apparent kinetics of highly reduced oxygen carriers with respect to oxidation using steam. This may also have some implications on defluidization tendency since the oxidation is exothermic, so this aspect can also be investigated.

Nomenclatures

A	Attrition rate based on investigation in the customized jet cup device
AHA	Associative hydrogen adsorption
AR	Air reactor
AU	After-used
A_{tot}	Initial attrition rate observed during the whole hour of observation
A_{30-60}	Attrition rate observed during the last 30 minutes into observation
$\bar{b}$	average stoichiometric coefficient metal oxides divided with that of reacting gas
$\overline{C_g}$	molar gas concentration around particles (vol.% or mol m^{-3})
C_{eq}	molar gas concentration at equilibrium (vol.% or mol m^{-3})
CGS	Changing grain size model
CLC	Chemical looping combustion
CLG	Chemical looping gasification
CLOU	Chemical looping with oxygen uncoupling
CLR	Chemical looping reforming
CLWS	Chemical looping water splitting
DIA	Dynamic image analysis
DHA	Dissociative hydrogen adsorption
E_a	activation energy (kJ mol^{-1})
FC	Freshly calcined
FO	Fully oxidized
FR	Fuel reactor
$f(\alpha)$	Solid-state kinetic formula in derivative form
$g(\alpha)$	Solid-state kinetic formula in integrated form
$k(T)$	temperature-dependent rate constant (s^{-1})
k_0	pre-exponential factor (s^{-1})
M_O	molecular weight of oxygen (16 gram/mol)
m_{ox}	mass of a fully oxidized sample (gram)
MR	moderately reduced
$\dot{n}$	molar flow (mol/second)
OC	Oxygen carrier

OCAC	Oxygen carrier aided combustion
OE	Oxygen exchange
p_{H_2}	hydrogen partial pressure (atm)
p_{H_2O}	steam partial pressure (atm)
r_i	reactivity of oxygen carrier *i* (s^{-1})
r_c	char conversion rate (s^{-1})
P	Perimeter of equivalent circle with the same surface area as the particles
Ps	Actual perimeter of particles
R	Universal gas constant (8.314 kJ/mol.K)
R_O	maximum observable oxygen transfer capacity (wt.%)
r_{OC}	average initial radius of the oxygen carrier particles (m)
R^2	Pearson correlation coefficient
SR	substantially reduced
S-Q	semi-quantitative
t	time (second)
T	temperature (K or °C)
T_m	melting point (°C)
U	fluidizing velocity (m/s)
U_{mf}	minimum fluidizing velocity (m/s)
X_c	fraction of char conversion
$x_{c,min}$	particle width/characteristic size
$x_{Fe,max}$	Feret diameter
x_i	molar fraction of species i
α	solid conversion degree based on active oxygen
δ	difference between experimental and model-calculated reactivity values
γ_i	gas yield of component *i*
ρ_m	molar density of gas (mol/m^3)
ω	mass conversion degree

References

1. Agache, I. *et al.* Climate change and global health: A call to more research and more action. *Allergy Eur. J. Allergy Clin. Immunol.* **77**, 1389–1407 (2022).
2. Dey, R. & Lewis, S. C. Natural disasters linked to climate change. in *The Impacts of Climate Change: A Comprehensive Study of Physical, Biophysical, Social, and Political Issues* 177–193 (Elsevier Inc., 2021). doi:10.1016/B978-0-12-822373-4.00004-5.
3. Ghazali, D. A. *et al.* Climate change impacts on disaster and emergency medicine focusing on mitigation disruptive effects: An international perspective. *Int. J. Environ. Res. Public Health* **15**, 1–13 (2018).
4. Luo, J. *et al.* Advances in subsea carbon dioxide utilization and storage. *Energy Rev.* **2**, 100016 (2023).
5. Rydén, M., Hanning, M. & Lind, F. Oxygen Carrier Aided Combustion (OCAC) of wood chips in a 12 MWth circulating fluidized bed boiler using steel converter slag as bed material. *Appl. Sci.* **8**, (2018).
6. Yu, Z. *et al.* Iron-based oxygen carriers in chemical looping conversions: A review. *Carbon Resour. Convers.* **2**, 23–34 (2019).
7. Julio, A. A. V., Castro-Amoedo, R., Maréchal, F., González, A. M. & Escobar Palacio, J. C. Exergy and economic analysis of the trade-off for design of post-combustion CO2 capture plant by chemical absorption with MEA. *Energy* **280**, (2023).
8. Jongpitisub, A., Siemanond, K. & Henni, A. *Simulation of Carbon-Dioxide-Capture Process using Aqueous Ammonia*. *Computer Aided Chemical Engineering* vol. 37 (Elsevier, 2015).
9. Grönkvist, S., Bryngelsson, M. & Westermark, M. Oxygen efficiency with regard to carbon capture. *Energy* **31**, 3220–3226 (2006).
10. Saghafifar, M., Schnellmann, M. A. & Scott, S. A. Limits of performance of chemical looping air separation in packed bed coupled with electricity production. *Int. J. Greenh. Gas Control* **118**, 103668 (2022).
11. Moghtaderi, B. Application of chemical looping concept for air separation at high temperatures. *Energy and Fuels* **24**, 190–198 (2010).
12. Staničić, I., Mattisson, T., Backman, R., Cao, Y. & Rydén, M. Oxygen carrier

aided combustion (OCAC) of two waste fuels - Experimental and theoretical study of the interaction between ilmenite and zinc, copper and lead. *Biomass and Bioenergy* **148**, (2021).

13. Thunman, H., Lind, F., Breitholtz, C., Berguerand, N. & Seemann, M. Using an oxygen-carrier as bed material for combustion of biomass in a 12-MWth circulating fluidized-bed boiler. *Fuel* **113**, 300–309 (2013).
14. Störner, F., Lind, F. & Rydén, M. Oxygen carrier aided combustion in fluidized bed boilers in Sweden—review and future outlook with respect to affordable bed materials. *Appl. Sci.* **11**, (2021).
15. Duan, L. & Li, L. *Oxygen-Carrier-Aided Combustion Technology for Solid-Fuel Conversion in Fluidized Bed*. *Oxygen-Carrier-Aided Combustion Technology for Solid-Fuel Conversion in Fluidized Bed* (2023). doi:10.1007/978-981-19-9127-1.
16. Vos, Y. De *et al.* Development of stable oxygen carrier materials for chemical looping processes—A review. *Catalysts* **10**, (2020).
17. Adánez, J. *et al.* Selection of oxygen carriers for chemical-looping combustion. *Energy and Fuels* **18**, 371–377 (2004).
18. Bartocci, P., Abad, A., Flores, A. C. & de las Obras Loscertales, M. Ilmenite: A promising oxygen carrier for the scale-up of chemical looping. *Fuel* **337**, 126644 (2023).
19. Mattisson, T. Materials for Chemical-Looping with Oxygen Uncoupling. *ISRN Chem. Eng.* **2013**, 1–19 (2013).
20. Mattisson, T., Lyngfelt, A. & Leion, H. Chemical-looping with oxygen uncoupling for combustion of solid fuels. *Int. J. Greenh. Gas Control* **3**, 11–19 (2009).
21. Liu, F., Liu, J. & Yang, Y. Review on the Theoretical Understanding of Oxygen Carrier Development for Chemical-Looping Technologies. *Energy and Fuels* **36**, 9373–9384 (2022).
22. Qasim, M., Ayoub, M., Ghazali, N. A., Aqsha, A. & Ameen, M. Recent Advances and Development of Various Oxygen Carriers for the Chemical Looping Combustion Process: A Review. *Ind. Eng. Chem. Res.* **60**, 8621–8641 (2021).
23. Daneshmand-Jahromi, S., Sedghkerdar, M. H. & Mahinpey, N. A review of chemical looping combustion technology: Fundamentals, and development of

natural, industrial waste, and synthetic oxygen carriers. *Fuel* **341**, 127626 (2023).

24. Abad, A., Mattisson, T., Lyngfelt, A. & Johansson, M. The use of iron oxide as oxygen carrier in a chemical-looping reactor. *Fuel* **86**, 1021–1035 (2007).
25. Mattisson, T., Lyngfelt, A. & Cho, P. The use of iron oxide as an oxygen carrier in chemical-looping combustion of methane with inherent separation of CO2. *Fuel* **80**, 1953–1962 (2001).
26. Zornoza, B., Abad, A., Mendiara, T. & Izquierdo, M. T. Iron-based oxygen carrier particles produced from micronized size minerals or industrial wastes. *Powder Technol.* **396**, 637–647 (2022).
27. Adánez, J. & Abad, A. Chemical-looping combustion: Status and research needs. *Proc. Combust. Inst.* **37**, 4303–4317 (2019).
28. Cabello, A., Mendiara, T., Teresa Izquierdo, M., García-Labiano, F. & Abad, A. Energy use of biogas through chemical looping technologies with low-cost oxygen carriers. *Fuel* **344**, 128123 (2023).
29. Goel, A., Ismailov, A., Moghaddam, E. M., He, C. & Konttinen, J. Evaluation of low-cost oxygen carriers for biomass chemical looping gasification. *Chem. Eng. J.* **469**, 143948 (2023).
30. Chen, P., Sun, X., Gao, M., Ma, J. & Guo, Q. Transformation and migration of cadmium during chemical-looping combustion/gasification of municipal solid waste. *Chem. Eng. J.* **365**, 389–399 (2019).
31. Egüez, A. Compliance with the EU waste hierarchy: A matter of stringency, enforcement, and time. *J. Environ. Manage.* **280**, 111672 (2021).
32. Purnomo, V. *et al.* Performance of iron sand as an oxygen carrier at high reduction degrees and its potential use for chemical looping gasification. *Fuel* **339**, (2023).
33. Ksepko, E., Klimontko, J. & Kwiecinska, A. Industrial wastewater treatment wastes used as oxygen carriers in energy generation processes A green chemistry approach. *J. Therm. Anal. Calorim.* **138**, 4247–4260 (2019).
34. Leion, H. *et al.* Use of CaMn0.875Ti0.125O3 as oxygen carrier in chemical-looping with oxygen uncoupling. *Energy and Fuels* **23**, 5276–5283 (2009).
35. Markström, P., Berguerand, N. & Lyngfelt, A. The application of a multistage-bed model for residence-time analysis in chemical-looping combustion of solid fuel. *Chem. Eng. Sci.* **65**, 5055–5066 (2010).

36. Purnomo, V., Mei, D., Soleimanisalim, A. H., Mattisson, T. & Leion, H. Effect of the Mass Conversion Degree of an Oxygen Carrier on Char Conversion and Its Implication for Chemical Looping Gasification. *Energy and Fuels* **36**, 9768–9779 (2022).
37. Adánez-Rubio, I., Ruiz, J. A. C., García-Labiano, F., de Diego, L. F. & Adánez, J. Use of bio-glycerol for the production of synthesis gas by chemical looping reforming. *Fuel* **288**, 119578 (2021).
38. Purnomo, V., Yilmaz, D., Leion, H. & Mattisson, T. Study of defluidization of iron- and manganese-based oxygen carriers under highly reducing conditions in a lab-scale fluidized-bed batch reactor. *Fuel Process. Technol.* **219**, 106874 (2021).
39. Zhang, S. *et al.* Effect of calcination condition on the performance of iron ore in chemical-looping combustion. *Fuel Process. Technol.* **203**, 106395 (2020).
40. Ilham, Z. Chapter 3 - Biomass classification and characterization for conversion to biofuels. in *Value-Chain of Biofuels* 69–87 (Elsevier Inc., 2022). doi:10.1016/b978-0-12-824388-6.00027-0.
41. Rydén, M., Leion, H., Mattisson, T. & Lyngfelt, A. Combined oxides as oxygen-carrier material for chemical-looping with oxygen uncoupling. *Appl. Energy* **113**, 1924–1932 (2014).
42. Hallberg, P. *et al.* Experimental investigation of CaMnO3-δ based oxygen carriers used in continuous chemical-looping combustion. *Int. J. Chem. Eng.* **2014**, (2014).
43. Zafar, M. Q. ul I. Oxygen Carriers Materials for Chemical-Looping Technologies -Reactivity and Kinetics. *Chalmers University of Technology* (2007).
44. Di Giuliano, A., Lucantonio, S. & Gallucci, K. Devolatilization of residual biomasses for chemical looping Gasification in Fluidized Beds Made up of Oxygen-Carriers. *Energies* **14**, (2021).
45. Pragadeesh, K. S. & Sudhakar, D. R. Color Indistinction Method for the Determination of Devolatilization Time of Large Fuel Particles in Chemical Looping Combustion. *Energy and Fuels* **33**, 4542–4551 (2019).
46. Leion, H., Frick, V. & Hildor, F. Experimental method and setup for laboratory fluidized bed reactor testing. *Energies* **11**, (2018).
47. ASTM. D5757-95 A. Standard Test Method for Determination of Attrition and

Abrasion of Powdered Catalysts by Air Jets. *Annual Book of ASTM Standards* vol. 00 2–4 (1995).

48. Rydén, M., Moldenhauer, P., Lindqvist, S., Mattisson, T. & Lyngfelt, A. Measuring attrition resistance of oxygen carrier particles for chemical looping combustion with a customized jet cup. *Powder Technol.* **256**, 75–86 (2014).
49. Cocco, R. *et al.* Jet cup attrition testing. *Powder Technol.* **200**, 224–233 (2010).
50. Azimi, G., Keller, M., Mehdipoor, A. & Leion, H. Experimental evaluation and modeling of steam gasification and hydrogen inhibition in Chemical-Looping Combustion with solid fuel. *Int. J. Greenh. Gas Control* **11**, 1–10 (2012).
51. Leion, H., Lyngfelt, A., Johansson, M., Jerndal, E. & Mattisson, T. The use of ilmenite as an oxygen carrier in chemical-looping combustion. *Chem. Eng. Res. Des.* **86**, 1017–1026 (2008).
52. Schwebel, G. L., Sundqvist, S., Krumm, W. & Leion, H. Apparent kinetics derived from fluidized bed experiments for Norwegian ilmenite as oxygen carrier. *J. Environ. Chem. Eng.* **2**, 1131–1141 (2014).
53. He, F. *et al.* Biomass chemical-looping gasification coupled with water/CO2-splitting using NiFe2O4 as an oxygen carrier. *Energy Convers. Manag.* **201**, 112157 (2019).
54. Zhang, R., Wang, Q. H., Luo, Z. Y., Fang, M. X. & Cen, K. F. Competition and Inhibition Effects during Coal Char Gasification in the Mixture of H2O and CO2. *Energy & Fuels* **27**, 5107–5115 (2013).
55. Hüttinger, K. J. Mechanism of water vapor gasification at high hydrogen levels. *Carbon N. Y.* **26**, 79–87 (1988).
56. Hüttinger, K. J. & Merdes, W. F. The carbon-steam reaction at elevated pressure: Formations of product gases and hydrogen inhibitions. *Carbon N. Y.* **30**, 883–894 (1992).
57. Hedayati, A., Soleimanisalim, A. H., Mattisson, T. & Lyngfelt, A. Thermochemical conversion of biomass volatiles via chemical looping: Comparison of ilmenite and steel converter waste materials as oxygen carriers. *Fuel* **313**, 122638 (2022).
58. Guo, L., Zhong, S., Bao, Q., Gao, J. & Guo, Z. Nucleation and growth of iron whiskers during gaseous reduction of hematite iron ore fines. *Metals (Basel).* **9**, (2019).
59. Adánez, J. *et al.* Syngas production in a 1.5 kWth biomass chemical looping

gasification unit using Fe and Mn ores as the oxygen carrier. *Energy and Fuels* **35**, 17182–17196 (2021).

60. Imtiaz, Q., Armutlulu, A., Donat, F., Naeem, M. A. & Müller, C. R. Preventing Agglomeration of CuO-Based Oxygen Carriers for Chemical Looping Applications. *ACS Sustain. Chem. Eng.* **9**, 5972–5980 (2021).
61. Liu, P. S. & Chen, G. F. Making Porous Metals. in *Porous Materials* 21–112 (Elsevier Inc., 2014). doi:10.1016/b978-0-12-407788-1.00002-2.
62. Condori, O. *et al.* Biomass chemical looping gasification for syngas production using ilmenite as oxygen carrier in a 1.5 kWth unit. *Chem. Eng. J.* **405**, 126679 (2021).
63. Leion, H., Mattisson, T. & Lyngfelt, A. Use of ores and industrial products as oxygen carriers in chemical-looping combustion. *Energy and Fuels* **23**, 2307–2315 (2009).
64. Hatanaka, T. & Yoda, Y. Attrition of ilmenite ore during consecutive redox cycles in chemical looping combustion. *Powder Technol.* **356**, 974–979 (2019).
65. Berguerand, N. & Lyngfelt, A. The use of petroleum coke as fuel in a 10 kWth chemical-looping combustor. *Int. J. Greenh. Gas Control* **2**, 169–179 (2008).
66. Staničić, I. *et al.* Investigating the Interaction between Ilmenite and Zinc for Chemical Looping. *Energy and Fuels* (2023) doi:10.1021/acs.energyfuels.3c01052.
67. Fossdal, A. *et al.* Study of dimensional changes during redox cycling of oxygen carrier materials for chemical looping combustion. *Energy and Fuels* **29**, 314–320 (2015).
68. Sundqvist, S., Arjmand, M., Mattisson, T., Rydén, M. & Lyngfelt, A. Screening of different manganese ores for chemical-looping combustion (CLC) and chemical-looping with oxygen uncoupling (CLOU). *Int. J. Greenh. Gas Control* **43**, 179–188 (2015).
69. Hildor, F., Leion, H. & Mattisson, T. Steel Converter Slag as an Oxygen Carrier—Interaction with Sulfur Dioxide. *Energies* **15**, 1–29 (2022).
70. Moldenhauer, P., Rydén, M., Mattisson, T. & Lyngfelt, A. Chemical-looping combustion and chemical-looping with oxygen uncoupling of kerosene with Mn- and Cu-based oxygen carriers in a circulating fluidized-bed 300 W laboratory reactor. *Fuel Process. Technol.* **104**, 378–389 (2012).
71. Ma, Y. *et al.* Hierarchical nature of hydrogen-based direct reduction of iron

oxides. *Scr. Mater.* **213**, 114571 (2022).

72. Liu, F. *et al.* Attrition and attrition-resistance of oxygen carrier in chemical looping process – A comprehensive review. *Fuel* **333**, 126304 (2023).
73. Brown, T. A., Scala, F., Scott, S. A., Dennis, J. S. & Salatino, P. The attrition behaviour of oxygen-carriers under inert and reacting conditions. *Chem. Eng. Sci.* **71**, 449–467 (2012).
74. Feilen, H. M. Attrition Rate Of Oxygen Carriers In Chemical Looping Combustion Systems. (University of North Dakota, 2015).
75. Faust, R., Lamarca, I., Schaefer, A., Lind, F. & Knutsson, P. Magnetic properties of ilmenite used for oxygen carrier aided combustion. *Fuel* **340**, 127593 (2023).
76. Cáceres-Martínez, L. E., Guío-Pérez, D. C. & Rincón-Prat, S. L. Significance of the particle physical properties and the Geldart group in the use of correlations for the prediction of minimum fluidization velocity of biomass–sand binary mixtures. *Biomass Convers. Biorefinery* **13**, 935–951 (2023).
77. Ocanha, E. S., Zinani, F. S. F., Modolo, R. C. E. & Santos, F. A. Assesment of the effects of chemical and physical parameters in the fluidization of biomass and sand binary mixtures through statistical analysis. *Energy* **190**, (2020).
78. Eppala, V. C. R., Varghese, M. M. & Vakamalla, T. R. Effect of particle shape on the hydrodynamics of gas-solid fluidized bed. *Chem. Eng. Res. Des.* **189**, 461–473 (2023).
79. Faust, R. *et al.* Role of surface morphology on bed material activation during indirect gasification of wood. *Fuel* **333**, (2023).
80. Pei, Y., Hinchliffe, B. A. & Minelli, C. Measurement of the size distribution of multimodal colloidal systems by laser diffraction. *ACS Omega* **6**, 14049–14058 (2021).
81. Blott, S. J. & Pye, K. Particle shape: A review and new methods of characterization and classification. *Sedimentology* **55**, 31–63 (2008).
82. Fedunik-Hofman, L., Bayon, A. & Donne, S. W. Kinetics of solid-gas reactions and their application to carbonate looping systems. *Energies* **12**, (2019).
83. Mattisson, T., Johansson, M. & Lyngfelt, A. Multicycle reduction and oxidation of different types of iron oxide particles-application to chemical-looping combustion. *Energy and Fuels* **18**, 628–637 (2004).
84. Dueso, C., Thompson, C. & Metcalfe, I. High-stability, high-capacity oxygen

carriers: Iron oxide-perovskite composite materials for hydrogen production by chemical looping. *Appl. Energy* **157**, 382–390 (2015).

85. Liu, W. *et al.* Kinetics of the reduction of wüstite by hydrogen and carbon monoxide for the chemical looping production of hydrogen. *Chem. Eng. Sci.* **120**, 149–166 (2014).
86. Abdalazeez, A. *et al.* Syngas production from chemical looping gasification of rice husk-derived biochar using BaFe2O4 as an oxygen carrier. *J. Energy Inst.* **105**, 376–387 (2022).
87. Mendiara, T. *et al.* Reduction and oxidation kinetics of Tierga iron ore for Chemical Looping Combustion with diverse fuels. *Chem. Eng. J.* **359**, 37–46 (2019).
88. Moed, N. M., Chiang, M. H., Ku, Y. & Tseng, Y. H. Kinetics for chemical looping process with fabricated Fe2O3-CuO/Al2O3 oxygen carriers. *Chem. Eng. Sci.* **258**, 117730 (2022).
89. Abad, A. *et al.* Kinetics of redox reactions of ilmenite for chemical-looping combustion. *Chem. Eng. Sci.* **66**, 689–702 (2011).
90. Hamers, H. P., Gallucci, F. & van Sint Annaland, M. Reactivity of oxygen carriers for CLC in packed bed reactors under pressurized conditions. *Submitt. to Energy* 1–16 (2014).
91. S, S. N. Reduction of iron oxides by carbon in a circulating fluidized bed reactor. *Powder Technol.* **124**, 28–39 (2002).
92. Shahrestani, M. M. & Rahimi, A. Evolution, fields of research, and future of chemical-looping combustion (CLC) process: A review. *Environ. Eng. Res.* **19**, 299–308 (2014).
93. Mattisson, T. *et al.* Innovative oxygen carriers uplifting chemical-looping combustion,Chemical-looping combustion, natural gas, integrated project, oxygen carrier development. *Energy Procedia* **63**, 113–130 (2014).
94. Chen, Y. Y., Nadgouda, S., Shah, V., Fan, L. S. & Tong, A. Oxidation kinetic modelling of Fe-based oxygen carriers for chemical looping applications: Impact of the topochemical effect. *Appl. Energy* **279**, (2020).
95. Wei, Z. *et al.* Reduction kinetics of hematite ore fines with H2 in a rotary drum reactor. *Powder Technol.* **332**, 18–26 (2018).
96. Nasr, S. & Plucknett, K. P. Kinetics of iron ore reduction by methane for chemical looping combustion. *Energy and Fuels* **28**, 1387–1395 (2014).

97. Sedghkerdar, M. H., Karami, D. & Mahinpey, N. Reduction and oxidation kinetics of solid fuel chemical looping combustion over a core-shell structured nickel-based oxygen carrier: Application of a developed grain size distribution model. *Fuel* **274**, 117838 (2020).
98. Means, N. C. *et al.* Examining and modeling oxygen uncoupling kinetics of Cu-based oxygen carriers for chemical looping with oxygen uncoupling (CLOU) in a drop tube fluidized bed reactor. *Energy and Fuels* **33**, 5610–5619 (2019).
99. Ramezani, R., Felice, L. Di & Gallucci, F. A review of chemical looping reforming technologies for hydrogen production: recent advances and future challenges. *JPhys Energy* **5**, (2023).
100. Bale, C. W. *et al.* FactSage thermochemical software and databases, 2010-2016. *Calphad Comput. Coupling Phase Diagrams Thermochem.* **54**, 35–53 (2016).
101. Tang, Q. & Huang, K. Determining the kinetic rate constants of Fe3O4-to-Fe and FeO-to-Fe reduction by H2. *Chem. Eng. J.* **434**, 134771 (2022).
102. Safarian, S., Saryazdi, S. M. E., Unnthorsson, R. & Richter, C. Gasification of woody biomasses and forestry residues: Simulation, performance analysis, and environmental impact. *Fermentation* **7**, 1–14 (2021).
103. Yu, Q. *et al.* An Overview on the Conversion of Forest Biomass into Bioenergy. *Front. Energy Res.* **9**, 1–10 (2021).
104. Stolte, N., Yu, J., Chen, Z., Sverjensky, D. A. & Pan, D. Water-gas shift reaction produces formate at extreme pressures and temperatures in deep earth fluids. *J. Phys. Chem. Lett.* **12**, 4292–4298 (2021).
105. Lussier, M. G., Zhang, Z. & Miller, D. J. Characterizing rate inhibition in steam/hydrogen gasification via analysis of adsorbed hydrogen. *Carbon N. Y.* **36**, 1361–1369 (1998).
106. Voitic, G. & Hacker, V. Recent advancements in chemical looping water splitting for the production of hydrogen. *RSC Adv.* **6**, 98267–98296 (2016).